V

MD Simulations of Ganglioside-containing Membranes

Abstract

GM1 gangliosides bound to amyloid β-protein (GM1-Aβ) on a lipid membrane are considered as a seed for aggregation of Aβ in Alzheimer's disease, and the GM1-Aβ formation is dependent on the concentration of Chol in the membrane. To reveal a mechanism of the GM1-Aβ formation and the dependency on Chol, MD simulations were carried out for two GM1-containing membranes: GM1 /SM/Chol = 1/2/2 (model 1) and GM1/POPC = 1/4 (model 2). The results indicated that, in model 1, GM1 molecules were condensed and had strong interactions with each other through hydrogen bonds mostly among the glycan parts. In contrast, GM1 molecules in model 2 were scattered on the membrane surface and the number of the hydrogen bonds markedly decreased. That is, GM1 cluster appeared only in model 1. The GM1 cluster yielded water-depleted regions on the membrane surface. Moreover, negative charges due to sialic acids of the GM1 cluster show a regular pattern in their distribution, which is compatible with the interval of hydrogen bond acceptors or donors of the main chain atoms of Aβ peptides in the β-strand conformation. These results suggest that GM1 cluster has the ability to attract Aβ peptides and to provide a hydrogen bond template for tightly holding them. Chol seems to play a role in maintaining an adequate interval of GM1 molecules by occupying the interstitial space between GM1 molecules.

V.1 Introduction

Gangliosides are known to be associated with virus infections and nervous diseases.[83,84] A particularly well-known example is a direct interaction between the toxins secreted by *Vibrio cholerae* and GM1 gangliosides in intestine.[85] Furthermore, gangliosides are related to symptoms of many nervous diseases, such as Huntington's disease and Alzheimer's disease (AD).[74,75,86,87]

It was reported that aggregation of amyloid β-peptides (Aβ) in a human brain is an important risk factor for AD.[88] Moreover, recent studies revealed that toxic Aβs aggregated on lipid microdomains with highly condensed glycolipids (especially ganglioside), SM, and Chol.[74,83,88,89] Until now, a lot of evidences have been accumulated to indicate that Chol is essential in AD (see the review by Shobab *et al*).[90] Yanagisawa *et al.* detected monosialo-ganglioside GM1-bound Aβ in the brains of patients with AD, and they suggested that GM1-Aβ may act as a seed for the aggregation of Aβ.[83] Several subsequent *in vitro* studies supported their hypothesis, and much evidence has been accumulated.[74,75,86,87] Based on the results of spectroscopic and fluorescence *in vitro* and *in vivo* studies, Matsuzaki *et al.* demonstrated that a high concentration of Chol promoted the formation of GM1 clusters and GM1-Aβ[74], and they suggested that Aβ recognized a GM1 cluster. These studies indicate that the presence of highly condensed GM1 molecules is critical for the formation of GM1-Aβ. However, it remains unclear how Aβs assemble on GM1-containing Chol-rich membranes.

Here in this study, two GM1-containing membranes were modeled by GLYMM in which the ratios of lipids are GM1/SM/Chol = 1/2/2 (model 1) and GM1/POPC = 1/4 (model 2), and MD simulations were carried out to elucidate the mechanism of Aβs assembly on GM1-containing Chol-rich membranes. The results of the present study provide a reasonable explanation for why Aβ specifically recognizes a GM1 cluster and aggregates on GM1-containing membranes.

Previous studies indicated that the Aβ aggregation on the membranes was very sensitive to experimental conditions.[74] Hence, in this study, in order to reproduce these experiments, the model system were carefully constructed as strictly close to the experimental conditions as possible (lipid composition, temperature: 37 °C, and ion concentration: 150 mM NaCl). The lipid composition of model 1 has been often used as a raft-mimicking environment to enable Aβs to aggregate in many experimental studies.[88,89,91-93] Therefore, the results of the MD simulations in this study will be also quite informative in discussing a mechanism of the formation of a lipid microdomain and its molecular structure in detail.

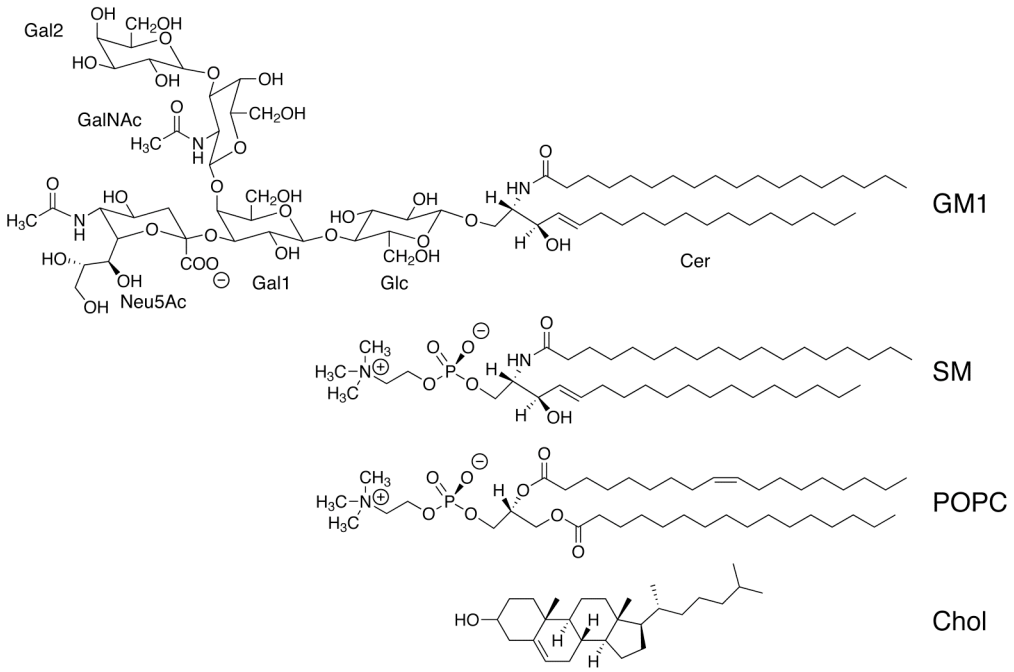

Figure 5.1 Chemical structures of the lipids used in this study.

V.2 Computational Details

Modeling of Model Membranes

The chemical structures used in this study are shown in Figure 5.1.

The molecular structures of Chol and N-acetylneuraminic acid (Neu5Ac) were constructed with the program *GaussView*. The electrostatic potentials of Chol and Neu5Ac were calculated by Gaussian 98 at the B3LYP/6-311+G** level and the B3LYP/6-31+G* level, respectively. The atomic charges were generated by fitting them to the electrostatic potentials with the *RESP* module of AMBER.[34] The force field parameters of Neu5Ac were transferred directly from the CHARMm force field parameters for small organic molecules.[94] Available parameters of alkanes and alkenes of the CHARMM27 force field parameters[43] for lipids were applied directly to the cholesterol. The missing parameters were created based on the analogy with available parameters.

Two model membranes were constructed with GLYMM. The coordinates and the number of GM1 molecules, water molecules, and ions were set equal between models 1 and 2. Then the models were solvated with water molecules so that the thicknesses of water molecule layers were 35 Å. Sodium ions were generated as counter ions against the minus charges of the GM1 molecules. Moreover, extra sodium ions and chloride ions were added to each system so that the concentration of NaCl became 0.15 M.

Initially, the two model membranes have the same size of 50.0 Å × 50.0 Å × 100.0 Å in x, y, and z directions, respectively. The two model membranes were pre-equilibrated at 310 K and 1 atm by 12 ns MD simulations. Model 1 resulted in 34.5 Å × 35.7 Å × 138.0 Å, and model 2 resulted in 46.8 Å × 45.2 Å × 88.5 Å. Then by duplicating the two obtained small model membranes in the x and y directions, two larger model membranes were created.

The sequence of the glycan parts of GM1 used in GLYMM was obtained from the database GLYCAN at KEGG.[50] Model 1 consisted of 48 GM1 molecules, 96 SM molecules, 96 Chol molecules (GM1/SM/Chol = 1/2/2), 19,292 water molecules, 52 sodium ions, and 4 chloride ions, and model 2 consisted of 48 GM1 molecules, 192 POPC molecules (GM1/POPC = 1/4), 19,292 water molecules, 52 sodium ions, and 4 chloride ions. The total numbers of atoms in model 1 and model 2 were 89,180 and 95,036, respectively. The final models resulted in 69.0 Å × 71.4 Å × 138.0 Å for model 1 and 93.6 Å × 90.4 Å × 88.5 Å for model 2.

Details of MD Simulations

The CHARMM27 force field parameters for lipids[43] and the CHARMm force field parameters for small organic molecules[94] were employed for all simulations. All simulations were performed with NAMD version 2.5.[69]

In the pre-equilibration stage for the quarter-size fragments of model membranes, energy minimization was initially carried out to remove unfavorable contact among molecules. Then the system was heated to 310 K, and 12 ns simulations with a constant pressure of 1 atm were executed to equilibrate the system at a constant temperature of 310 K. Before the MD simulations for the full-size model membranes, energy minimization was carried out to remove unfavorable contacts among molecules. Then the system was heated to 310 K, and 10 ns simulations were executed to equilibrate the system at a constant temperature of 310 K and a constant pressure of 1 atm.

A periodic boundary condition was applied, and the pressure and the temperature were kept constant by the Nosé-Hoover Langevin piston method in NAMD during the simulations. The cutoff distance of the vdW and the Coulomb potentials at the real space was set to 12 Å. The integration time step was 2 fs. Energy correction by the PME method was applied at 4 fs intervals to include the electrostatic contribution from the neighboring cells to the infinite distance into the electrostatic energy.

Analysis of MD Simulations

For analysis, the data were collected at 20 ps intervals during the last 5 ns MD simulations. The surfaces of the membranes were visualized by GRASP[95] to clarify the difference in morphology depending on the composition of the membrane. The order parameter was calculated by the following equation:

$$S_{CD} = \left| \frac{3\langle cos^2\theta \rangle - 1}{2} \right| \quad \text{..... (5.1)}$$

where θ means the average angle between each of the C-H bonds of CH_2 groups of lipids and the bilayer normal vector (z axis). The brackets denote the averaging over time and over all lipids. The mean square displacements were calculated using the *ptraj* module in AMBER to estimate the diffusion constants of lipids and Chol. The H-bonds were examined using the *ptraj* module in AMBER and the statistical program R.[70] H-bond score was defined as follows:

$$Hbond\ score = \sum_{Hbond} \frac{t_{Hbond}}{t_{MD}} * 100 \quad \text{..... (5.2)}$$

where t_{Hbond} and t_{MD} mean the time for keeping the H-bonds and the total time for collecting the data, respectively. The probability density of lipids and Chol around a reference Chol were measured with respect to both distance and orientation and were visualized using VMD. In order to account for the orientation dependency of molecular density around cholesterols, the coordinates of the trajectories were rotated so that all of the cholesterol molecules were fitted to the reference cholesterol. Then the 1.0 Å × 1.0 Å × 1.0 Å grids were generated around the reference Chol. Next, the atoms of the specified molecules were counted at each grid for all the trajectories and were averaged over time and the number of cholesterol molecules. The radial distribution functions were computed using the *ptraj* module of AMBER. The membrane surfaces colored by curvature were drawn by GRASP. B-factors of glycans were computed using the *ptraj* module of AMBER. Superimposed snapshot structures of a GM1 molecule in model 1 (Figure 5.8) were created by VMD.

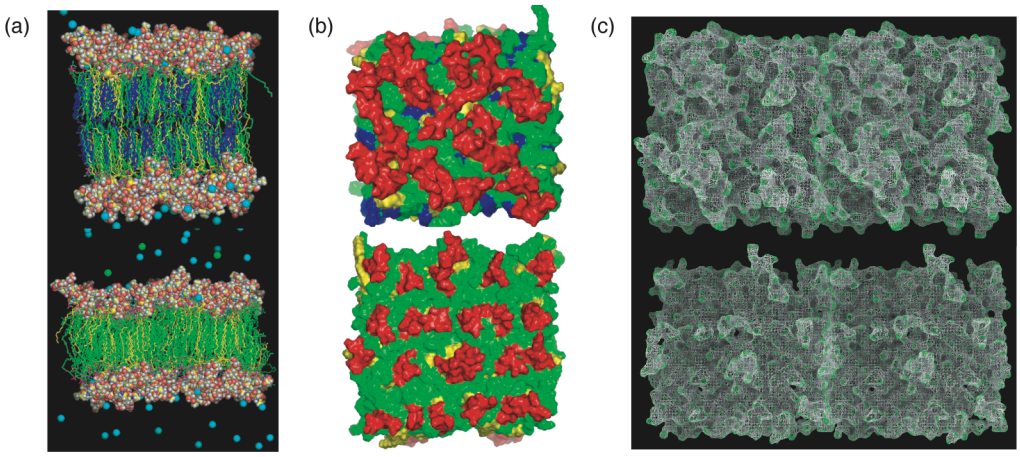

Figure 5.2 Snapshot structures of the membranes at 5 ns.

(a) Structure viewed from the side (upper: model 1, lower: model 2). The glycan parts of GM1 molecules and ions are represented as vdW spheres colored by atom types, and the other lipids are drawn as sticks colored by residue types (green: SM or POPC; blue: Chol; yellow: ceramide part of GM1). (b) Top views of the snapshot structures of the membranes colored by lipid types. The glycan parts of GM1 are colored red. (c) Top views of the membrane colored by the surface curvature. The molecular graphics in (a) and (b) were created by PyMOL, and those in (c) were drawn by GRASP.

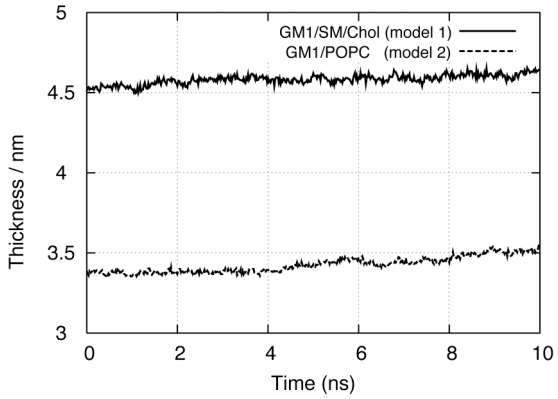

Figure 5.3 Thickness of the membranes during MD simulations.

The thickness is calculated from the P-P distance of SM or POPC.

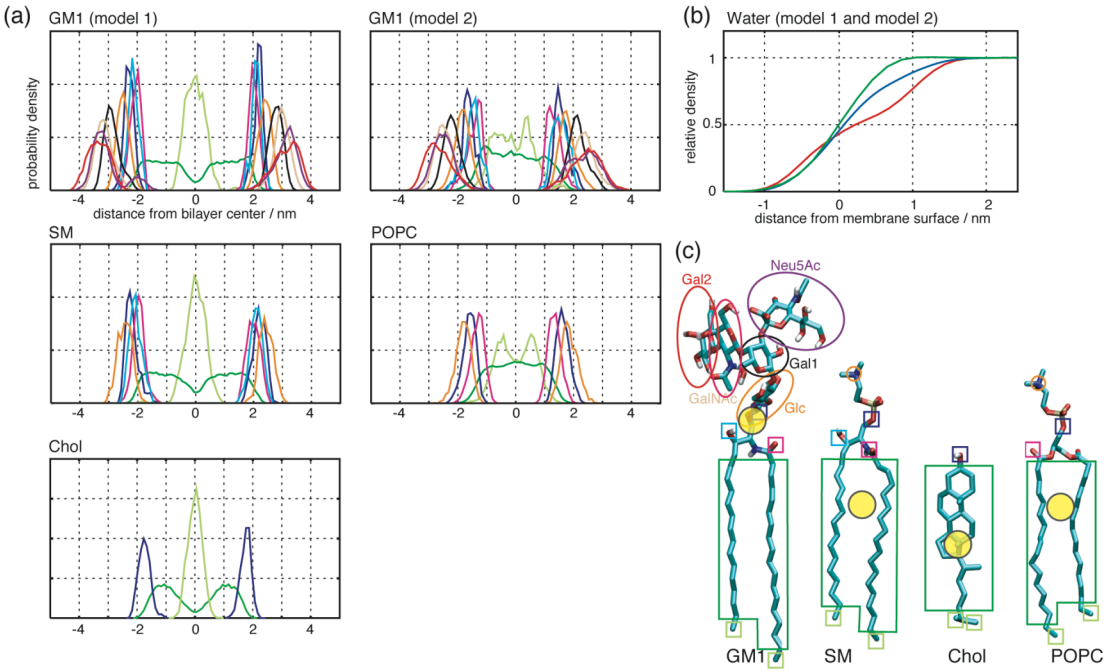

Figure 5.4 Distribution of molecules along the membrane normal.

(a) Probability densities of lipids (left column: model 1, right column: model 2). See boxes and ovals on the molecules in (c) for coloring. (b) Relative densities of water molecules (red line: model 1, blue line: model 2, green line: DPPG bilayer). Bulk density of water molecules is set to 1.0. (c) Molecular models of lipids and Chol. Boxes and ovals are in the same colors as (a). Yellow circles indicate the centers of mass of GM1, SM, and Chol.

V.3 Results

Overall Picture of the Membranes

Figure 5.2 shows snapshot structures of the two model membranes, in which a clear difference between the two membranes is observed in their appearance. Model 1 seems to be in a liquid-ordered (l_o) phase, where there is little overlap of alkyl chains between the upper and the lower leaflets, moreover the alkyl chains align vertically against the membrane surface. On the other hand, model 2 seems to be in an interdigitated-gel ($L_\beta I$) phase, where the lipids insert their alkyl chains into the opposite leaflet, and the thickness of the bilayer apparently decreases compared with model 1. Time-averaged thickness (P-P distance) of model 1 and model 2 was 46.0 ± 0.2 Å and 34.7 ± 0.3 Å, respectively (Figure 5.3). These results are compatible with the experimental facts that a GM1/SM/Chol membrane was in l_o phase[96] and a GM1/POPC membrane was in the LβI phase at 37 °C.[97] Moreover, some clusters of glycans and some grooves between the clusters can be seen in model 1, while the surface of model 2 is relatively flat and the glycan parts of GM1 are scattered on the membrane surface ((Figure 5.2 (b) and (c)).

Figure 5.4 shows the probability density functions of molecules along the membrane normal (z axis). Figure 5.4 (a) shows the shapes of the functions of lipids in model 1 are sharper than those in model 2, which indicates that lipids in model 1 are more highly ordered along the membrane normal direction than those in model 2. It should be noted that the distribution of phosphate ester oxygen of SM in model 1 has a shoulder at the maximum point of the distribution of Chol-O1, while such a peak are not observed in GM1 in model 1. This difference results from a strong attractive force between Chol and SM at their head groups. The distribution of the terminal methyl atoms of lipids in model 1 have only one sharp peak at the center of the membrane, while that of model 2 splits into two peaks. The single peak means that the upper and the lower leaflets of the membrane are clearly separated, while the double peak is indicative of interdigitation, as described in *Chapter III*. Figure 5.4 (b) shows the densities of water molecules relative to that of the bulk water. The curve indicates that water molecules in model 1 are excluded from the membrane surface on which glycans are highly concentrated. These results reveal that more hydrophobic environment was induced due to the formation of the cluster of glycans. The induced water-less-region is more clearly shown when comparing this results with the relative densities of water molecules of a DPPG bilayer after a 2 ns MD simulation (Figure 5.4 (b)).

Figure 5.5 (a) shows charge density profiles of model 1 and model 2 along the membrane normal. Both profiles have a single large negative peak at the membrane

surface due to the phosphate moieties of SM and POPC, followed by small positive peaks mainly due to the choline moieties of SM and POPC, and partially due to the sodium ions. A clear difference is the presence of the second large negative peak at the region distant from the surface in model 1, while in the model 2 the corresponding peak is almost diminished. This second negative peak is due to the carboxyl groups of Neu5Ac residues. Charge density profiles of POPC, DPPG, and DPPS bilayers after the 2 ns MD simulations do not exhibit such a second large negative peak (Figure 5.5 (b), the data were obtained from the simulations in *Chapter III*, and were calculated with the contribution from ions).

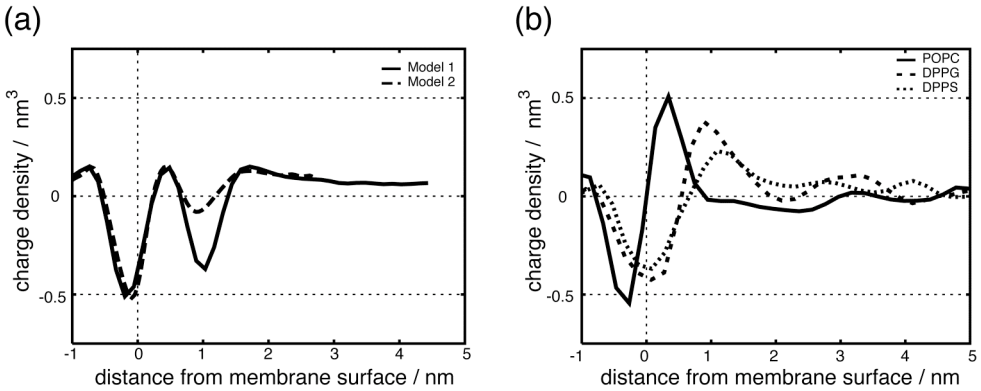

Figure 5.5 Charge density profiles at the water-membrane interfaces.

(a) Charge density profiles of model 1 and model 2. The solid and the dashed line indicate the results of model 1 and model 2, respectively. (b) Charge density profiles of POPC, DPPG, and DPPS bilayers after the 2 ns MD simulations along the membrane normal (z axis) measured from the bilayer surface.

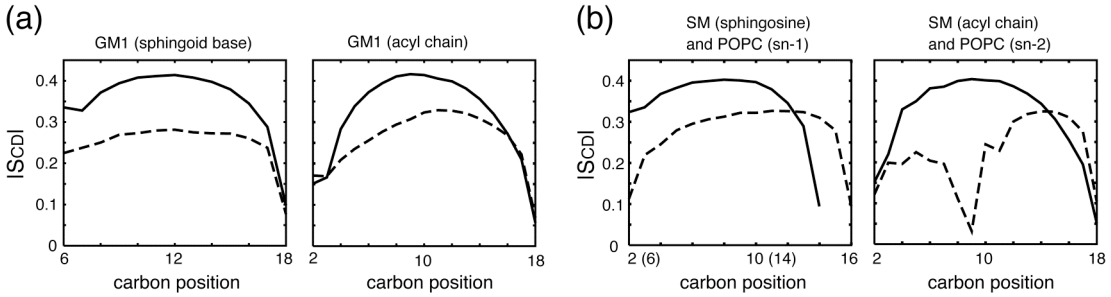

Figure 5.6 Order parameters of lipid tails of GM1, SM, and POPC.

The solid line and the dashed line show the results for model 1 and model 2, respectively. Parentheses at the abscissa in (b) mean the carbon position of sphingosine.

Lipid-Lipid Interactions

The order parameters, S_{CD}, of alkyl chains of lipids in the two models were calculated from our MD simulations (Figure 5.6), which clearly indicates that the lipid alkyl chains in model 1 become more highly ordered than those in model 2. High order parameter values of POPC around the terminal methyl groups indicate the interdigitation.

To examine how lipids interact with each other, we calculated scores of hydrogen bonds (H-bonds) (Table 5.1). In model 1, the phosphate groups (PO_4) of SM largely contribute to the H-bonds between lipids. More than 60% of the H-bonds between SM-SM attribute to the interactions between PO_4 and the ceramide backbone atoms (NH, OH, and C=O; hereafter referred as Cer). On the other hand, in SM-GM1 interaction, the H-bonds between PO_4-Cer are prominently decreased, while the H-bonds between PO_4-glycan and Cer-Cer are increased. As for GM1-GM1, almost all of the H-bonds are formed between glycans, particularly between Gal2-Gal2, whereas the H-bonds between Cer-Cer are scarcely observed. In model 2, the most frequently observed H-bonds are between PO_4-glycan in POPC-GM1, particularly between PO_4-Glc. The glycan-glycan interactions are mainly observed between GM1-GM1 also in model 2.

Table 5.2 shows the H-bond scores between lipids and Chol. The H-bonds between SM-Chol are formed preferentially between Cer residues, whereas the H-bonds between GM1-Chol have no preference. This result indicates that Chol prefers to make H-bonds with SM rather than GM1. Since no H-bond between Chol-Chol is observed in our simulation, the Chol-Chol interaction is concluded to be primarily hydrophobic.

Table 5.1 Scores of H-bonds between lipids

		PO_4 and sphingoid base					Glycan					
		OH-PO_4	OH-O=C	NH-PO_4	NH-OH	NH-O=C	Glc	Gal1	GalNAc	Neu5Ac	Gal2	Total
model 1	SM-SM	652 (50 %)	101 (8 %)	176 (13 %)	202 (16 %)	171 (13%)	NA	NA	NA	NA	NA	1301
	SM-GM1	114 (2 %)	37 (1 %)	9 (0 %)	717 (12 %)	749 (12%)	1792 (29 %)	1078 (18 %)	419 (7 %)	689 (11 %)	499 (8 %)	6104
	GM1-GM1	NA	7 (0 %)	NA	0	0	1150 (23 %)	489 (10 %)	905 (19 %)	956 (20 %)	1397 (29 %)	4905
model 2	PC-GM1	571 (7 %)	NA	801 (10 %)	NA	NA	2259 (27 %)	995 (12 %)	1499 (18 %)	976 (12 %)	1307 (16 %)	8408
	GM1-GM1	NA	0	NA	31 (1 %)	1 (0 %)	1015 (44 %)	255 (11 %)	520 (23 %)	165 (7 %)	321 (14 %)	2308

The score of H-bond is defined in the previous section. The scores of glycan are a sum of the scores of the glycan-head group interaction and the glycan-glycan one. Percentage ratios of H-bonds in each lipid pair (SM-SM, etc) are also shown in parentheses.

Table 5.2 Scores of H-bonds between lipids and hydroxyl group of cholesterols

	Cer – Chol	PO_4 – Chol	Glycan – Chol	Total
SM – Chol	1454 (57.4 %)	1079 (42.6 %)	NA	2533
GM1 – Chol	402 (47.3 %)	NA	447 (52.7 %)	849

The definition of the score is the same as Table 5.1.

Table 5.3 Lateral diffusion coefficients of lipids

	GM1	SM	POPC	Chol
Model 1	1.06	1.69	-	1.67
Model 2	1.96	-	2.64	-

Unit is 10^{-12} m^2/s ($\mu m^2/s$).

For investigating the lateral diffusion of lipids and Chol within the membrane plane, lateral diffusion constants, D_L, of GM1, SM, POPC, and Chol were calculated (Table 5.3) by the following equation:

$$D_L = \lim_{t\to\infty} \frac{1}{4t} \left\langle \sum_a (\mathbf{r}_a(t) - \mathbf{r}_a(0))^2 \right\rangle \quad \text{..... (5.3)}$$

where the brackets mean an ensemble average, $\boldsymbol{r_a(t)}$ represents an atom coordinate at time t. The calculated D_L indicates that the GM1 molecules in model 1 diffused much more slowly than that in model 2. Interestingly, the D_L of SM and Chol are approximately equal, although the molecular weight of Chol is much smaller than that of SM (Chol = 340.3, SM = 628.5). This suggests that SM and Chol laterally diffused together due to their strong intermolecular interactions.

Glycan-Glycan Interactions

The H-bond scores between the glycan parts of GM1 are shown in Table 5.4. A comparison of model 1 with model 2 reveals a large increase of H-bond scores among their terminal glycans (Gal2 and Neu5Ac) in model 1. Furthermore, sum of the scores over all glycan parts is much greater than those between non-glycans (Tables 5.1, 5.2). In both model 1 and 2, Gal1 at the branching core of GM1 remarkably contributed to intramolecular H-bonds. Previous NMR experiments of GM1 micelles pointed out that the Neu5Ac residues formed intramolecular H-bonds with the GalNAc.[98] In MD

simulations in this study, the intramolecular H-bonds between GalNAc-Neu5Ac are also frequently observed in both models.

It has been reported that the number of Neu5Ac is closely related to the Aβ aggregation.[74,87,99] Hence, in order to analyze the distributions of Neu5Ac, radial distribution functions (RDF) of carboxyl oxygen atoms of Neu5Ac residues of GM1 were examined as shown in Figure 5.7. The RDF in model 1 has a peak at 14 Å, while that of model 2 peaked at 10 Å in the full-size model membranes. Furthermore, the maximum of the RDF in model 1 is 2.5-times larger than the bulk density of Neu5Ac, while that of model 2 is no more than 1.5-times. This indicates a high condensation of Neu5Ac in model 1. Moreover, in the quarter-size model membranes, the characteristic peak is also observed at 7 Å (Figure 5.7 (b)). See Figure 5.8 for a detailed view of the complex structure of glycans.

Table 5.4 Scores of H-bonds between glycan

			Donor				
			Glc	Gal1	Neu5Ac	GalNAc	Gal2
Model 1	Acceptor	Glc	88.4 (ND)	77.2 (1216.0)	44.8 (200.0)	27.6 (211.2)	91.2 (0.0)
		Gal1	43.6 (509.2)	14.4 (ND)	160.8 (84.4)	206.4 (709.6)	172.8 (0.0)
		Neu5Ac	4.8 (10.8)	60.0 (1237.6)	290.8 (ND)	83.2 (52.0)	210.0 (4.4)
		GalNAc	6.4 (11.6)	47.6 (460.4)	202.4 (1320.4)	314.8 (ND)	273.6 (702.4)
		Gal2	112.0 (0.0)	173.2 (0.4)	536.4 (86.0)	333.6 (590.4)	410.0 (ND)
Model 2	Acceptor	Glc	131.2 (ND)	78.8 (1114.8)	152.4 (96.8)	15.2 (208.0)	67.6 (0.0)
		Gal1	18.0 (472)	17.2 (ND)	132.0 (43.2)	27.2 (887.2)	33.2 (0.0)
		Neu5Ac	45.6 (15.6)	78.8 (1331.2)	146.8 (ND)	112.8 (80.0)	63.2 (2.8)
		GalNAc	29.2 (35.2)	7.2 (451.2)	33.2 (1030.0)	21.2 (ND)	32.0 (656.0)
		Gal2	115.2 (0.0)	20.0 (0.0)	100.0 (62.0)	30.0 (695.6)	76.0 (ND)

The definition of the score is the same as Table 5.1 (Scores for the intramolecular H-bonds are given in parentheses).

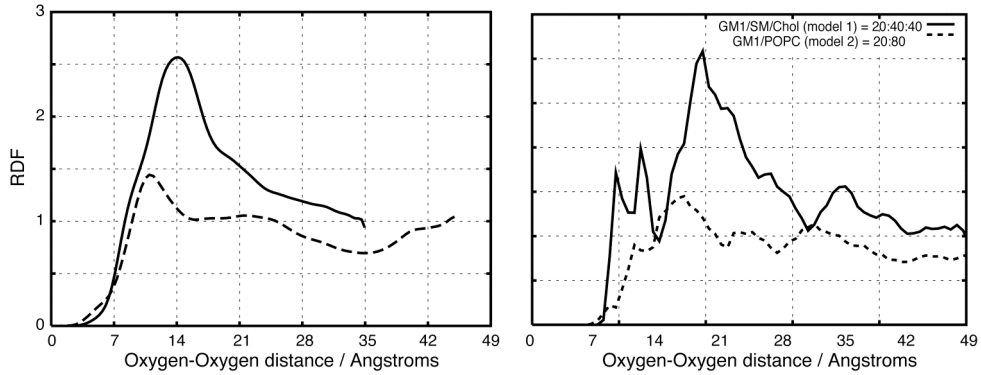

Figure 5.7 Radial distribution functions of carboxyl oxygen atoms of Neu5Ac.

Model 1: solid line, model 2: dashed line. Left: results of full size membranes. Right: results of quarter size membranes.

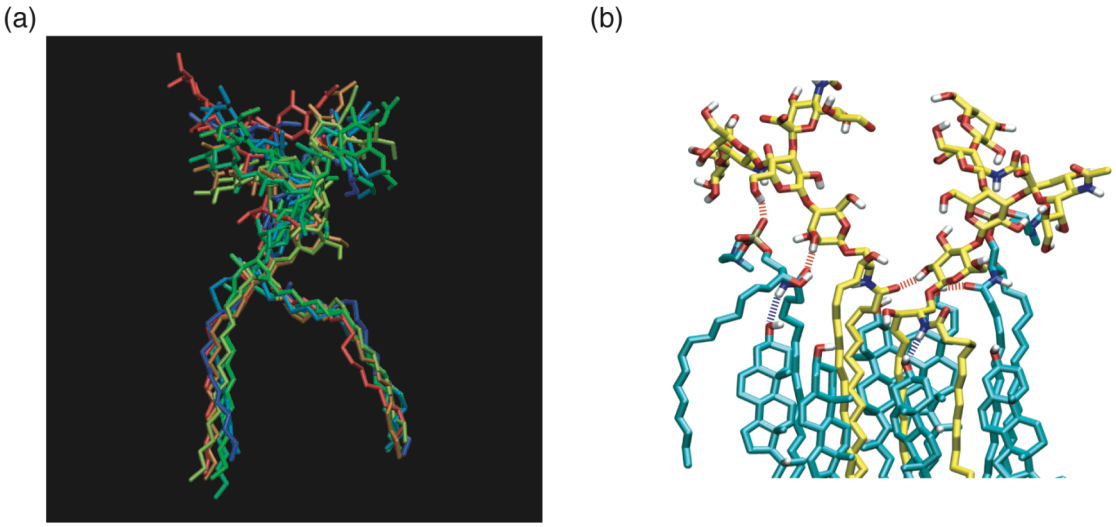

Figure 5.8 Fluctuation and interactions of GM1.

(a) Superimposed snapshot structures of a GM1 molecule in model 1 obtained at 0.8-ns intervals during the last 5 ns of simulation. GM1 molecules are represented by sticks. The hydrogen atoms are not shown for clarity. (red: 0 ns, orange: 0.8 ns, tan: 1.6 ns, light green: 2.4 ns, green: 3.2 ns, sky blue: 4.0, blue: 4.8 ns) (b) Snapshot structure of a GM1 dimer surrounded by Chol and SM. The non-polar hydrogen atoms are omitted for clarity. The dashed lines represent the hydrogen bonds (red: OH-O, blue: NH-O). The carbon atoms of GM1 are colored yellow, and those of other lipids are colored cyan. The oxygen, nitrogen and polar hydrogen atoms are colored red, blue, and white, respectively.

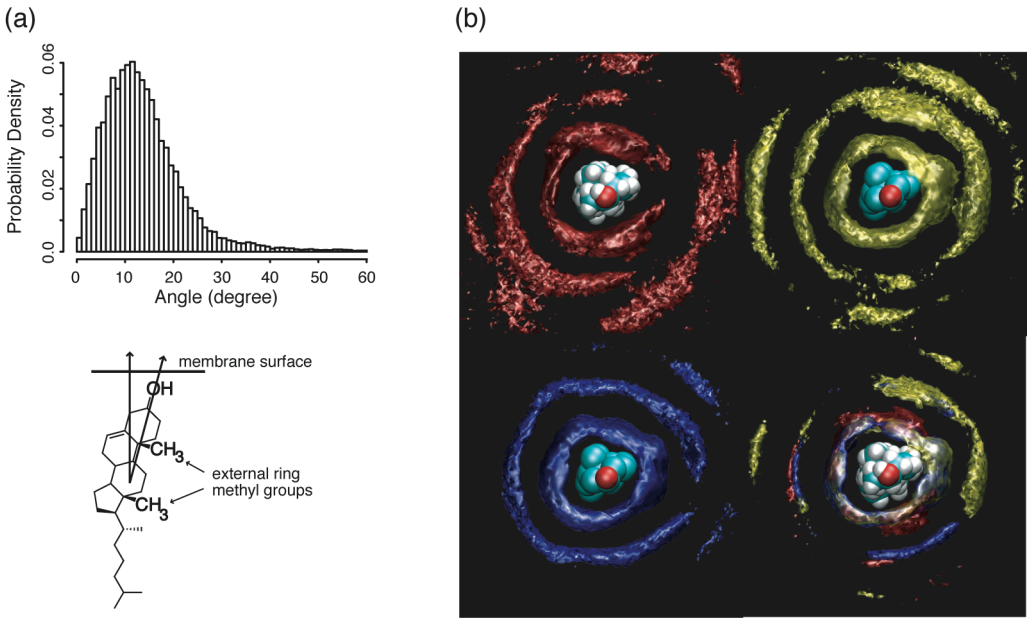

Figure 5.9 Cholesterol in GM1/SM/Chol bilayer.

(a) Upper: Histogram of orientations of the principal axis of the Chol molecule with respect to the angle against the bilayer normal, lower: the most probable orientation of Chol. The membrane normal vector and the principal axis of Chol are also shown. (b) Probability density functions of lipid chains around cholesterols with respect to distance and orientation. The iso-surface plot at the value of 1.5 (red: Chol-Chol, yellow: Chol-GM1, blue: Chol-SM, hydrogen atoms are omitted for clarity in Chol-GM1 and Chol-SM). The superimposed iso-surface plot at the value of 2.0 is shown at the lower right.

V.4 Discussions

Evaluation of MD Simulations of GM1-containing Membranes

It is very important for an MD simulation to reproduce the previous experimental and computational results precisely.

The time-averaged thickness of model 1 is 46.0 ± 0.2 Å and that of model 2 is 34.7 ± 0.3 Å (Figure 5.3), which appears in a clear difference in Figure 1 (a). Each thickness is consistent with the experimentally measured thickness of an SM bilayer with Chol and a pure PC bilayer, 46 ~ 56 Å and 35 Å, respectively.[1] In views of structures, model 1 can be concluded to result in l_o phase, while model 2 results in an interdigitated phase (Figure 5.2 and 5.4). Mehlhorn et al. reported that GM1 caused the interdigitation of many kinds of phosphoglycerides including egg PC.[97] Moreover, Ryhanen et al. revealed that the increase in membrane surface charge density was a factor to induce the interdigitation of PC.[100] Furthermore, an electron microscopic study indicated that GM1 was dispersed in PC bilayers.[101] Our simulation well reflects these experimental results.

MD simulations in the current study indicate that Chol molecules show an ordering effect on the alkyl chains of GM1 (Figure 5.6), which have been pointed out by a lot of previous experiments and in *Chapter IV* in this thesis. Moreover, the tilt angles of Chol with respect to the bilayer normal and the distributions of lipids around Chol (Figure 5.9) are compatible with other computational results.[24]

The calculated lateral diffusion coefficients, D_L, of the lipids in model membranes are also consistent with the previous experimental results (Table 5.3).[102] In the MD simulations in the current study, the lipids in the interdigitated phase diffused more rapidly than those in l_o phase. D_L value of fluorescence labeled GM1 (10 mol %) in DMPC bilayers in L_α phase at 308 K was 0.47 $\mu m^2/s$, while D_L of pure DMPC determined under the same condition was 1.6 $\mu m^2/s$.[103] Because the D_L of DMPC was 4~6 $\mu m^2/s$ in L_α phase[104] and about 10^{-3} $\mu m^2/s$ in L_β phase,[105] incorporation of GM1 into a membrane in L_α phase is unlikely to dramatically change the D_L such as the L_α to L_β phase transition. In fact, Schram et al. reported that the interdigitation did not affect the translational diffusion of lipids.[106] Since an NMR experiment revealed that the D_L of POPC in L_α phase was 6.0 $\mu m^2/s$,[107] the D_L value of POPC with 20 mol % GM1 calculated in the current study is reasonable (Table 5.3). Dehydration of a bilayer was reported to suppress the lateral diffusion of lipids.[108] As shown in Figure 5.4, the model 1 membrane is more dehydrated than the model 2, which can be a factor of slow lipid diffusion in model 1.

Judging from these consistencies of the simulation results with the previous experiments, our MD simulations are considered to correctly reproduce the model membranes.

Characteristics of GM1 Cluster

In GM1 cluster, many intra- and intermolecular H-bonds were observed (Tables 5.1, 5.2 and 5.4). In particular, the remarkable increase was observed in the number of H-bonds between glycan-glycan moieties. In contrast, H-bonds among non-glycan head groups in the GM1 cluster were scarcely observed. The number of H-bonds among glycans in GM1-GM1 interactions in model 1 is two-times larger than that in model 2, which is particularly prominent at the terminal glycan residues: Neu5Ac, GalNAc, and Gal2. These H-bonds stabilized the clustering of glycan portions of GM1, which decreased the fluctuation of glycans (Table 5.5). However, it could not be determined from the data whether the increase of H-bonds resulted from the GM1 clustering or the GM1 cluster results from the increase of H-bonds.

Dense clustering of the glycans excluded water molecules on the water-membrane interface (Figure 5.4 (b)). The decrease of the density of water on the surface is more discerned clearly when compared with acidic phospholipid DPPG bilayer (Figure 5.4). Figure 5.4 shows that galactose are rich in these water-less-regions. Galactose is known to have a hydrophobic face that can interact with hydrophobic or aromatic amino acid residues of proteins.[109-111] In addition, as shown in Figure 5.5, a negatively charged region is also produced due to the GM1 cluster. Taking these results into account, a GM1 cluster has a quite unique feature that the surface has a strong hydrophobicity but contains a negatively charged region.

Effects of Cholesterol on GM1 Cluster Formation

The results of the MD simulations provide a clue as to why Chol promotes the formation of the GM1 cluster.

As for polar interactions, many H-bonds between lipids and Chol are observed in model 1 (Tables 5.2). The contribution of Chol to the total H-bonds score in model 1 is 20%. The increase of H-bonds from Chol contributes to stabilize the head groups of lipids, which makes lipids close to each other and possibly prevents the interdigitation. In fact, Chachaty et al. demonstrated using the synchrotron x-ray diffraction that Chol eliminated the interdigitated phase in SM/Chol membranes,[112] and Tiemey et al. also indicated that Chol inhibited the interdigitation induced by the exposure to a high concentration of ethanol.[113] Here in the MD simulations, more H-bonds between

Chol-SM are formed compared with Chol-GM1 (Table 5.2). As for non-polar hydrophobic interactions, MD simulations have revealed that Chol induces the strong solvation shells around itself formed by the surrounding alkyl chains of SM and GM1 (Figure 5.9 (b)). However, a clear difference between Chol-SM and Chol-GM1 are not observed in the non-polar interactions. Hence, considering the polar and the non-polar interactions together, Chol is concluded to form a more stable complex with SM than GM1.

In general, the complex formation relates to the mutual relative positions of center of mass (COM). When COMs of two objects are close with each other, the complex is readily formed because of the force working on the two objects. The COM of Chol and SM are positioned almost at the same height, but that of GM1 is positioned higher (Figure 5.4 (c)). The same height of the COMs indicates that Chol-SM can attract each other more strongly in the lateral direction than Chol-GM1, That is, SM molecules are attracted to Chol more tightly compared with GM1, which will result in the preference for the formation of the Chol-SM complex. Therefore, Chol is concluded to tend to form a complex with SM more frequently, which would cause the exclusion of GM1 from Chol-SM complexes, consequently inducing the clustering of GM1 molecules. Further investigation will be needed to confirm this speculation.

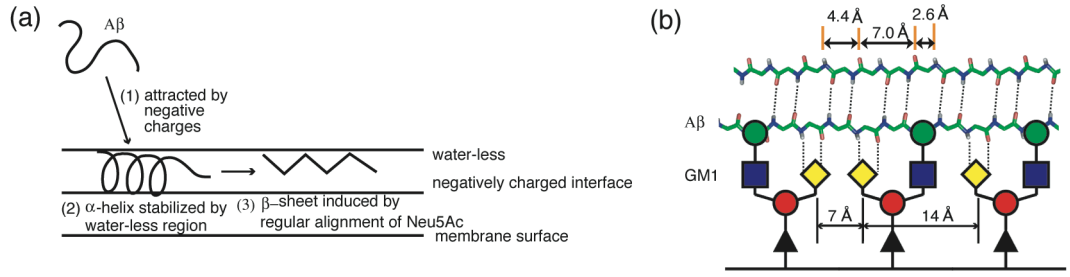

Figure 5.10 Proposed mechanism of GM1-Aβ formation.

(a) Schematic representation of the proposed mechanism of GM1-Aβ formation. (b) A proposed aggregation mechanism of Aβ peptides on GM1 molecules through H-bonds.

Proposed Binding Mechanism of Amyloid β Peptides with GM1 Cluster

Previous experimental studies revealed the importance of the number of Neu5Ac for Aβ binding to ganglioside-containing membranes.[74,86,99] The results in the current study reveal that Neu5Ac of GM1 appear at the intervals of 7 or 14 Å in GM1 cluster (Figure 5.7). To identify structural relationship of the Neu5Ac distribution with Aβ aggregation, an ideal β-strand conformation of Aβ was modeled and analyzed. Surprisingly, the intervals of Neu5Ac are compatible with the intervals of the appearance of H-bond acceptors or donors at the main chain of the Aβ peptide in the β-strand conformation

(Figure 5.10). This suggests that Aβ peptides can recognize Neu5Ac residues aligned at the constant intervals and will change their conformation into the β-strand conformation. That is, the alignment of Neu5Ac can function as a template for the conformational change of Aβ peptides into the β-strand through the H-bonds between Neu5Ac residues and peptides (Figure 5.10). In fact, the X-ray crystallographic structure of cholera toxin, which is a famous protein interacting with GM1, suggested that cholera toxin recognizes GM1 through H-bonds between the main chain atoms and Neu5Ac residues.[85] Furthermore, the cholera toxin has a β-strand conformation at the binding site for Neu5Ac.

It was also reported that Aβ in an α-helical conformation was bound to a GM1-including membrane composed of GM1/SM/Chol (1/2/2, same as model 1 used in the current study), when Aβ/GM1 molar ratio was low.[89,114] Many studies pointed out that a membrane-binding peptide is generally attracted electrostatically to the acidic lipids on a membrane.[115-117] In fact, Aβ can be bound to the bilayers composed of acidic phospholipids such as PS and PG.[74,118] However, it should be noted that it is only a ganglioside-containing membrane that has a capability of binding with Aβ under physiological ionic strength (150 mM NaCl or 100 mM sodium phosphate) and neutral pH range.[74,119] In order to reveal why Aβ is bound only to ganglioside-containing membrane under physiological condition, the results of MD simulations of POPC, DPPS, and DPPG bilayers have been compared with the results (Figure 5.5). The results show that the charge density profiles of both DPPS and DPPG membranes were quite similar to neutral POPC membranes. Sodium ions canceled out most of the negative charges, which resulted in producing the membranes being almost neutral near the membrane surface. However, as shown in Figure 5.5, the GM1-containing membranes have the negatively charged region away from the membrane surface due to Neu5Ac moieties, especially GM1/SM/Chol membrane keeps high electric negativity even under the physiological condition. This negative charge will become the attractive force for Aβ to bind with the ganglioside-containing membranes. This explanation can also give a satisfactory reason for the increase of the binding constant of Aβ with the number of Neu5Ac.

In addition to the presence of strong negative charges, the GM1 cluster also provides hydrophobic environment on the membrane surface. Hydrophobic environment stabilizes α-helical conformation of Aβ by promoting intramolecular H-bonds in the peptide backbone.[120-123] Therefore, the hydrophobic region induced by the GM1 cluster will be an important factor for stabilizing the α-helical conformation of Aβ on the GM1-containing membrane surface. McLaurin et al. demonstrated that the α-helical content of Aβ on GM1-containing membranes was retained at 1.0 M NaCl and pH 7.0 while the β-strand content decreased remarkably.[86] Furthermore, Katagiri et al. revealed,

using quantum chemical calculations, that H-bonds from water molecules stabilized a peptide in β-strand conformation more than α-helical one, when the sequence of the peptide was the same.[122] These results suggest the α-helical conformation of Aβ is mainly stabilized by water-less, hydrophobic interactions and the β-strand conformation is stabilized by H-bonds from Neu5Ac.

To sum up, (1) Aβ is initially attracted by the strong negative charges on the GM1 cluster, then (2) stabilized by the interaction with the hydrophobic regions in the α-helix-rich conformation, and (3) converted into the β-strand-rich conformation, led by the Neu5Ac residues of GM1 aligned at the appropriate intervals on the membrane.

V.5 Conclusion

MD simulations of two GM1-containing membranes, GM1/SM/Chol = 1/2/2 (model 1) and GM1/POPC = 1/4 (model 2), reveal that (1) GM1 cluster makes hydrophobic but locally negatively charged regions on the membrane surface due to the condensation of the glycan parts of GM1. This hydrophobicity is advantageous for binding Aβs in the α-helix rich conformation on the GM1-containing membranes. (2) Neu5Ac residues of GM1 molecules appear at the intervals of 7 or 14 Å in model 1, while GM1 molecules are scattered on the membrane surface in model 2. These intervals are compatible with the intervals of the appearance of the main chain atoms of Aβ in the β-strand conformation. This regular alignment of H-bond donors or acceptors on the GM1 cluster is highly influential and will induce the conversion of Aβs from the α-helix rich conformation to the β-strand rich one. This conversion into the β-strand rich conformation is speculated to be a trigger for the Aβs aggregation on the ganglioside-containing and Chol-rich membranes.

VI

MD Simulations of Small G-proteins in Solution

Abstract

MD simulations were performed for the Mg^{2+}-free small guanine nucleotide-binding proteins (GNBPs): Ras, Rho, Rab, Arf, and Ran in complex with GDP to investigate the effects of Mg^{2+} ions on the GNBPs' structure. The results indicated that all Mg^{2+}-free GNBPs formed a groove between the switch region and the nucleotide-binding site. In some GNBP families, the release of Mg^{2+} was reported to play an important role in binding the guanine nucleotide-exchanging factor (GEF) promoting the GDP/GTP exchange reaction. Interestingly, the grooves, which appeared in the MD simulations, were similar to the grooves experimentally observed in the GNBP-GEF complex. MD simulations of the Mg^{2+}-bound GNBPs were also calculated for comparison. No groove was observed in the Mg^{2+}-bound form. Moreover, p*Ka* calculations were carried out to investigate the effects of Mg^{2+} ion on the protonation states of amino acid residues of GNBPs. The results revealed that the p*Ka* values of the residues in the vicinity of Mg^{2+} binding site were so affected that some residues changed their protonation states by the removal of Mg^{2+} ion. These results demonstrate a regulatory role of Mg^{2+} ion to prepare a template for the GEF binding.

VI.1 Introduction

Small guanine nucleotide-binding proteins (GNBPs) are molecular switches or timers that control a variety of cellular functions.[46,124] Small GNBPs constitute the Ras superfamily comprising five subfamilies: Ras, Rho, Rab, Arf, and Ran.[46] The homology in amino acid sequences among the families is approximately 30 %, and the members of the five subfamilies have a common core structure, which contains five α–helices and six β–sheets (Figure 6.1). Distinct from the three small GNBP subfamilies, the Arf and the Ran subfamilies have an additional seventh β–sheet. Moreover, four motifs are conserved in all small GNBPs; a phosphate-binding loop (P-loop) (GXXXXGKS/T), Switch 1 (YXPT), Switch 2 (DTAG), and a guanine-binding loop (NKXD and SAK).

Despite their similarities, both in the structure and the sequence, their functions extend widely, which has been revealed with the genetic, cell biological and biochemical approaches: the Ras family regulates cell proliferation and differentiation,[125,126] morphology,[127] and apoptosis;[128] the Rho family regulates cytoskeletal rearrangement involved in morphology, movement, and behavior;[129,130] the Rab and Arf families regulate endoplasmic vesicle trafficking;[131] and the Ran family regulates nucleoendoplasmic transport.[132] The GNBP cycles between the inactive GDP-bound and the active GTP-bound states, therefore, small GNBPs are called "switching proteins". In this switching cycle, the two proteins, guanine nucleotide exchange factors (GEFs) and GTPase activating proteins (GAPs), promote the switching of the GNBP. Furthermore, GDP dissociation inhibitors (GDIs) are also involved in the switching cycle,[46] where they inhibit the GDP-GTP exchange and keep the GNBP inactive. GEFs accelerate the exchange of GDP for GTP, that is, the dissociation of GDP from a GNBP and the association of GTP to the GNBP. When the GNBP becomes active, the GNBP can interact with the proteins in the downstream of the signal transduction. GAPs promote GTP hydrolysis, which return GNBPs to the inactive state.

Many studies have been carried out to reveal the mechanism of the GEF-mediated exchange reaction. Some kinetic studies demonstrated that GEF-mediated exchange reactions involved GNBP-GEF-nucleotide ternary intermediate formation;[133,134] thus the following mechanism was proposed in Scheme 6.1:

Scheme 6.1. GEF-mediated exchange reaction.

$$\text{GNBP-GDP} \leftrightarrow \text{GNBP-GDP-GEF} \leftrightarrow \text{GNBP-GEF} \leftrightarrow \text{GNBP-GTP-GEF} \leftrightarrow \text{GNBP-GTP}$$

The ternary complex has a low affinity for a nucleotide; moreover, it initiates a fast conformational change, inducing the dissociation of the nucleotide. This leads to the

formation of a nucleotide-free binary complex. Several crystallographic structures of the nucleotide-free binary GNBP-GEF complexes were reported, in which GEFs placed their helices or loops to the Mg^{2+}-binding site.[135-138] The Mg^{2+}-binding site is usually surrounded with Switch 1, Switch 2, and P-loop, which suggests the disturbance of the Mg^{2+} coordination has a crucial effect on the GEF-mediated GDP/GTP exchange reaction.

Mg^{2+} ion is an essential cofactor for all the small GNBPs. In the GDP- and the GTP-bound forms, the Mg^{2+} ion is bound with the protein in an octahedral coordination. The binding affinity of Mg^{2+} ion for GNBPs is low when the Mg^{2+} ion concentration decreases in the micromolar level.[139] It is also known that excess Mg^{2+} ions inhibit the GDP dissociation from GNBPs and, therefore, prevent the binding of GTP with GNBPs.[139-143] The removal of Mg^{2+} ions by chelating agents increases the GEF activity and their affinity.[133,140] Since the equilibrium constant for the binding of Mg^{2+} ion to GNBP can be measured in experiments,[139] it is natural to consider that not only Mg^{2+}-bound GNBPs are observed but also Mg^{2+}-free ones are found in the solution. The above experimental data suggest that Mg^{2+}-free GNBPs would have some physiological functions. However, little is known about the state of Mg^{2+}-free GNBPs. Recently, the crystallographic structure of the Mg^{2+}-free RhoA with GDP was reported,[144] in which the switch 1 region was dislocated and became distant from the nucleotide-binding site. The study revealed that the Mg^{2+} ion could regulate the conformation of RhoA, which suggested that Mg^{2+}-free RhoA could be an intermediate of the GEF-mediated GDP/GTP exchange reaction. In addition, it was reported that the release of Mg^{2+} ion preceded the GDP dissociation in the GDP/GTP exchange reaction in Rac, a member of the Rho family.[145] Thus, it is suggested that the Mg^{2+} ion is released before the GDP/GTP exchange reaction in the Rho family. These studies allowed us to speculate that Mg^{2+} ions might regulate conformations of other GNBPs, yet details of their conformations in the absence of Mg^{2+} ion remain unclear.

To investigate the features of the Mg^{2+}-free GNBPs' conformations, MD simulations were performed for the Mg^{2+}-bound and the Mg^{2+}-free GNBPs in complex with GDP. As a result, the Mg^{2+}-free conformations were found similar to GNBPs in the GEF-binding state. The critical roles of the Mg^{2+} ion in determining the conformations of GNBPs and in binding of GEFs to GNBPs are discussed. The results in this study suggest that the GDP dissociation occurs by a stepwise mechanism, where the emergence of the Mg^{2+}-free semiopen GDP form leads to the formation of the GEF-GNBP binary complex.

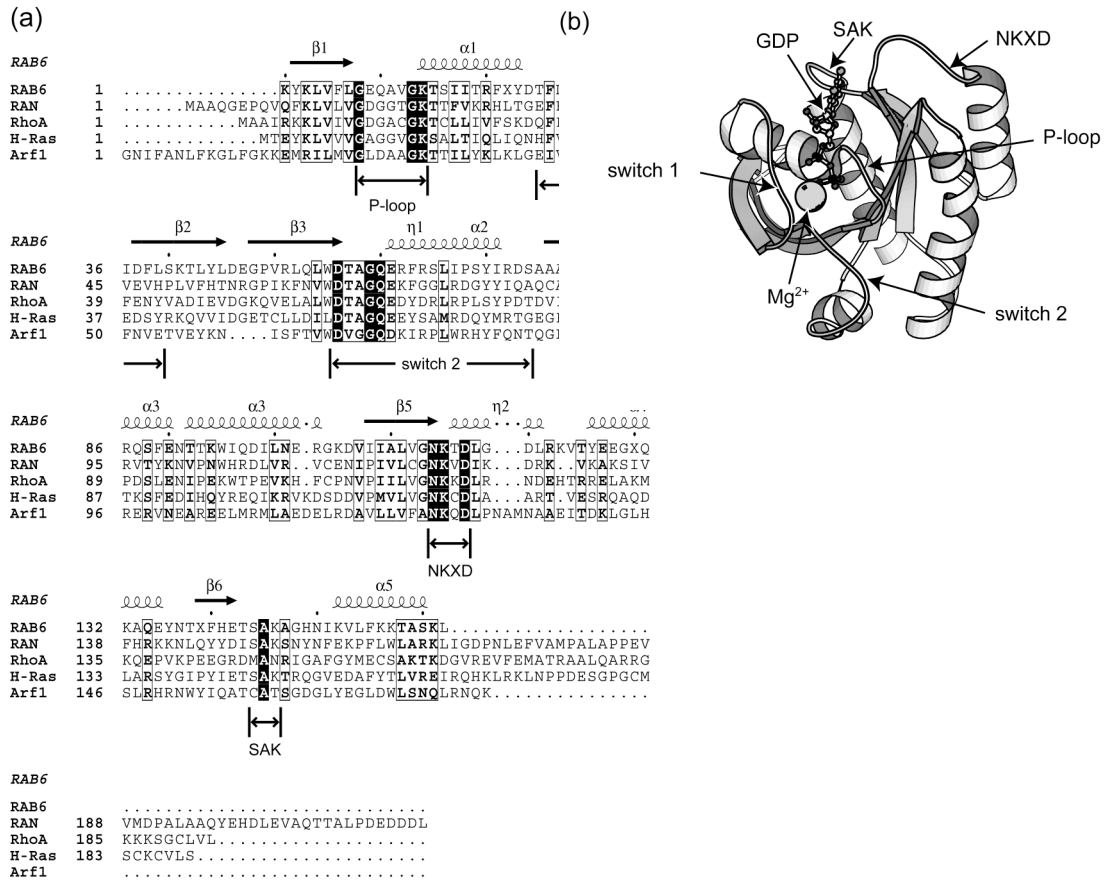

Figure 6.1 Small G-proteins used in this study.

(a) Full length sequences of Rab6, Ran, RhoA, H-Ras, and Arf1. Consensus sequences: P-loop, Switch 1, Switch 2, and the guanine-binding loops (NKXD and SAK) are labeled. (b) Core structure common to small G-proteins (H-Ras structure depicted as a representative). Mg^{2+} ion is shown as a sphere. GDP is shown by a ball-and-stick representation.

VI.2 Computational Details

Modeling of Initial Structures

The structures of the Mg^{2+}-bound small GNBPs used in our simulations were obtained from the X-ray crystallographic structures of the truncated GNBPs in complex with both GDP and Mg^{2+} ion (H-Ras, Protein Data Bank (PDB) code is 4Q21,[146] containing 166 residues; RhoA, 1FTN,[147] containing 177 residues; Rab6, 1D5C,[148] containing 162 residues; chain A of Arf1, 1HUR,[149] containing 180 residues; chain B of Ran, 1BYU,[150] containing 215 residues). The structures of the Mg^{2+}-free GNBPs were constructed by removing the Mg^{2+} ion manually from the respective structures. Because the side chain of the arginine residue at the C-terminus of the H-Ras protein was built by the *LEaP* module of AMBER 8,[34] the truncated H-Ras has a total of 167 residues. The mutated residue (Asn25) of the RhoA protein was converted to the wild type (Phe25). The selenomethionine residues of the Rab6 protein were also returned to the normal methionines.

Considering the effect of removing the Mg^{2+} ion on the protonation state of the residues in proteins, p*Ka* calculations were carried out using the p*Ka* calculation program MCCE[151] software to examine the p*K*a values for all the titratable residues (see the calculated p*K*a values in Table 6.1). The protonation states at pH 7.0 were determined for all the titratable residues, and these residues were renamed to represent the protonation state according to their residue types used in AMBER: that is, GLU, ASP, and HIS were renamed into GLH, ASH, and HIP, respectively, when the p*K*a values were greater than 7.0, and HIS and LYS were renamed to HIE or HID and LYN when less than 7.0.

Finally, each complex was solvated with TIP3P water molecules[78] in a cubic box of about 70 Å × 70 Å × 70 Å by the *LEaP* module. Then, counterions were placed around the proteins so that the net charge was zero in each system, using the *LEaP* module.

Details of MD Simulations and Analyses

The MD simulations were performed with the *pmemd* module of AMBER 8. All atom ff02 force field[36] was used in all MD simulations. A periodic boundary condition was applied, and the pressure was kept constant during the simulations using the Berendsen algorithm.[152] The temperature was kept constant at 300 K. The procedure performed in our simulations was as follows. The system was minimized by the steepest descent method without any constraint for bond length. The additional

minimization was executed by the conjugate gradient method. The system was gradually heated from 0 K to 300 K for 56 ps and then kept at 300 K until the atom density of the system was equilibrated. The non-bonded electrostatic energy was calculated by the PME method. The cutoff distance in real space for Coulomb and van der Waals forces was 15 Å. To reduce the computational effort, only bond lengths, involving hydrogen atoms, were constrained by the SHAKE method,[153] which allowed the integration time step to be 2 fs. The simulation time was 3.0 ns for each model.

To investigate the influence of the specific protonation states deduced from the p*Ka* calculations on GNBPs' conformation, the MD simulations were carried out at the default protonation state of AMBER at pH 7.0, where Asp, Glu, Lys, and Arg residues were ionized and His residues were neutral. The MD simulations described above were repeated for these calculations.

The trajectories were analyzed with the *CARNAL* and the *ptraj* modules in AMBER. The mass-weighted B-factors were calculated for each residue by the following equation:

$$B_{res} = \sum_{a=N_{res}}^{N_{res}-1} m_a B_a \Big/ \sum_{a=N_{res}}^{N_{res}-1} m_a$$

$$B_a = \frac{8}{3}\pi^2 \langle \delta \mathbf{r}_a^2 \rangle, \quad \delta \mathbf{r}_a = \mathbf{r}_a - \langle \mathbf{r}_a \rangle_t \qquad \text{..... (6.1)}$$

where *a* and *res* symbolize the atom number and the residue number, respectively; N_{res} represents the number indicating the first atom in the residue *res*; $\mathbf{r}_a$ and m_a represent the coordinate and the mass of atom *a*, respectively. The brackets represent the time average. The B-factors were analyzed using the statistical program R,[70] in which the sample cross correlations between the calculated B-factor and the crystallographic temperature factor were calculated by the following equation:

$$R = \frac{C(y,z)}{C(y,y)C(z,z)}$$

$$C(y,z) = \frac{1}{T}\sum_{t=1}^{T}(y_t - \mu_y)(z_t - \mu_z) \qquad \text{..... (6.2)}$$

where *R* and *C* represent a sample cross correlation and a sample cross covariance, respectively; *T* represents the number of residues; y and z denote the data sets containing B-factors and temperature factors of all the residues; μ_y and μ_z represent the

averages of y and z, respectively. *R* can vary in the range from -1 to 1; hence, the two variables, y and z, have a strong positive correlation when *R* is close to 1.

All the molecular graphics were produced using the programs MolScript,[2] MOLMOL,[154] and GRASP.[95] Solvent accessible surface areas were calculated with MOLMOL.

VI.3 Results

p*Ka* Values with and without Mg^{2+} Ion

In four of the five GNBPs (except for Arf1), the removal of Mg^{2+} ion extremely affected the p*Ka* value of an Asp residue in the vicinity of the GDP-binding site (shown in Table 6.1: Asp57 in H-Ras; Asp59 in RhoA; Asp66 in Rab6; Asp65 in Ran). These Asp residues are close to the phosphate moiety of GDP and are buried in the proteins. This environment would cause the Asp residues to be neutral, because the neutral state of an Asp or a Glu residue is more stable in the electrically negative and hydrophobic environment. In the case of Arf1, Glu54 is noticeably affected, and its p*Ka* value is larger than 7.0. Although Asp67 in Arf1 is slightly affected, it remains to be acidic.

In addition, Lys residues in the P-loop are also affected except for Arf1 (Lys16 in H-Ras; Lys18 in RhoA; Lys24 in Rab6; Lys23 in Ran). In particular in RhoA and Rab6, the difference is so large that the net charge of each Lys changes positive to neutral.

Hence the removal of the Mg^{2+} ion would change the protonation state of amino acid residues around the GDP-binding site. The protonation state of the Asp or the Lys residue near the GDP-binding site will influence the switch conformations.

In contrast, the p*Ka* values of Arg, Glu (except for Arf1), and His residues are independent of the removal of Mg^{2+} ion. Nevertheless, some of them have unique p*Ka* values that are clearly different from their intrinsic p*Ka* values in the water. This means that some residues are in the different protonation state from the AMBER default one. These results indicate that the protonation states of amino residues are quite sensitive to their surrounding environment. Each protein has a unique three-dimensional structure, which provides amino acids with a unique environment. Therefore, p*Ka* calculations may be important for the molecular modeling to reproduce the protein dynamics accurately with MD simulations.

Table 6.1 p*Ka* values in each GNBP calculated by MCCE

Arg

H-Ras			RhoA			Rab6			Arf1			Ran		
#	Mg(+)	Mg(-)	#	Mg(+)	Mg(-)	#	Mg(+)	Mg(-)	#	Mg(+)	Mg(-)	#	Mg(+)	Mg(-)
41	>14.0	>14.0	5	13.8	13.8	30	>14.0	>14.0	19	NA	NA	29	NA	NA
68	>14.0	>14.0	68	13	13	61	13.2	13.2	75	12.4	12.4	56	13.6	13.5
73	13.9	13.9	70	NA	NA	72	>14.0	>14.0	79	13.8	13.9	76	12.6	12.6
97	>14.0	>14.0	122	>14.0	>14.0	74	13.3	13.3	97	>14.0	>14.0	95	13.2	13.2
102	>14.0	>14.0	128	>14.0	>14.0	82	13.4	13.4	99	>14.0	>14.0	106	>14.0	>14
123	>14.0	>14.0	129	13	13	96	>14.0	>14.0	104	13.5	13.6	110	NA	NA
128	12.4	12.4	145	13.5	13.5	113	>14.0	>14.0	109	NA	NA	129	>14.0	>14
135	13.4	13.4	150	13.9	13.9	132	NA	NA	117	13.5	13.5	140	13.8	13.8
149	13.3	13.4	168	NA	NA				149	12.7	12.7	166	>14.0	>14
161	>14.0	>14.0	176	13.8	13.8				151	>14.0	NA			
164	>14.0	>14.0												

Asp

H-Ras			RhoA			Rab6			Arf1			Ran		
#	Mg(+)	Mg(-)	#	Mg(+)	Mg(-)	#	Mg(+)	Mg(-)	#	Mg(+)	Mg(-)	#	Mg(+)	Mg(-)
30	3.1	3.3	13	6.7	6.6	34	3.4	3.5	26	3.9	4	18	5.2	4.9
33	3.8	4.4	28	2.6	2.6	37	4.2	4.3	67	2.8	5	65	3.6	>14.0
38	3.8	4	45	5.0	5.1	47	3.7	4.2	72	5.2	5.2	77	3.1	3.1
47	1.1	1.1	49	3.2	3.3	56	4.5	4.5	93	4.2	4.3	91	6.1	6.1
54	2.6	2.8	59	7.6	>14.0	66	5.8	>14.0	96	6.6	6.7	107	2.4	2.3
57	>14.0	>14.0	65	4.3	4.3	83	2.8	2.7	114	4.1	4.1	125	3.6	3.6
69	3.9	3.9	67	2.7	2.8	92	8.6	8.4	118	3.7	3.6	128	3.4	3.4
92	3.9	4.3	76	3.8	3.8	108	6	5.9	129	3.1	3.1	148	1.2	1.2
105	5.2	5.2	78	4.1	4.1	116	4.3	4.3	141	4.0	4	171	2.9	2.9
107	3.1	3.1	87	13.5	13.7	127	2	2	164	4.7	4.7	190	3.3	3.3
108	4.1	4.1	90	3.7	3.8	130	3.3	3.3	171	4.6	4.5	200	4.7	4.8
119	1.7	1.8	120	2.9	3							211	4.9	4.9
132	4.0	3.9	124	2.6	2.7							213	4.7	4.7
154	3.5	3.5	146	5.0	5							214	5.2	5.2
			165	1.8	1.8							215	4.3	4.3

His

H-Ras			RhoA			Rab6			Arf1			Ran		
#	Mg(+)	Mg(-)	#	Mg(+)	Mg(-)	#	Mg(+)	Mg(-)	#	Mg(+)	Mg(-)	#	Mg(+)	Mg(-)
27	7.8	8	105	6	6	151	0.8	0.8	80	6.4	6.4	30	2.3	2.3
94	6.4	6.4	126	6.2	6.2	159	6	6	146	6	6	48	<0.0	<0.0
166	7.3	7.4							150	5.9	5.9	53	6	6.1
												105	5.6	5.6
												139	2.5	2.5
												199	6.2	6.2

Glu

H-Ras			RhoA			Rab6			Arf1			Ran		
#	Mg(+)	Mg(-)	#	Mg(+)	Mg(-)	#	Mg(+)	Mg(-)	#	Mg(+)	Mg(-)	#	Mg(+)	Mg(-)
3	4.5	4.5	32	4.6	4.7	19	6.5	6	17	4.5	4.6	6	3.8	3.8
31	5.4	5.5	40	4.0	4.2	57	5.1	5.1	41	4.5	4.5	34	1.9	2.1
37	5.4	6.4	47	6.4	6.4	71	3.4	3.4	54	1.6	9.9	36	4.0	4
49	2.8	2.8	54	4.3	4.3	100	3.2	3.2	57	4.8	4.7	46	3.3	3.9
62	4.6	4.7	64	3.7	3.9	112	3.9	3.9	98	3.6	3.5	70	12.8	11.8
63	4.4	4.5	93	5.4	5.3	137	4	4	102	2.6	2.6	113	4.5	4.5
76	2.3	2.3	97	4.7	4.7	138	3.5	3.5	105	3.7	3.7	158	4.7	4.7
91	3.5	3.5	102	1.0	1.4	145	4.5	4.5	106	6.3	6.3	175	4.3	4.3
98	2.4	2.4	125	4.9	4.9	152	6	6	113	2.3	2.3	186	2.9	3
126	3.1	3.1	130	3.2	3.3				115	4.8	4.8	198	3.0	3
143	5.4	5.4	137	2.5	2.5				138	4	4	202	4.2	4.2
153	2.9	2.9	142	2.7	2.7				168	3.7	3.7	212	5.0	5
162	5.2	5.2	143	6.0	6									
			158	1.0	1.2									
			169	3.7	3.7									
			172	5.3	5.3									

Lys

H-Ras			RhoA			Rab6			Arf1			Ran		
#	Mg(+)	Mg(-)	#	Mg(+)	Mg(-)	#	Mg(+)	Mg(-)	#	Mg(+)	Mg(-)	#	Mg(+)	Mg(-)
5	10.7	10.7	6	12	12	11	11	11	10	11.1	11.1	12	9.5	9.4
16	8.8	11.7	7	11.2	11.2	13	7.4	7.3	15	10.4	10.4	23	1.2	5.2
42	11	11.1	18	4	9.2	24	<0.0	9.5	16	11.4	11.4	28	10.0	10.3
88	13.4	13.5	27	11.5	11.6	51	9.4	9.4	30	10.3	11.9	37	12.1	12.1
101	9.4	9.4	51	10.9	10.9	104	12.1	12.3	36	11.2	11.4	38	10.5	10.4
104	12.5	12.5	98	11.8	11.9	115	11.2	11.2	38	9.5	9.5	60	10.1	10.1
117	10	10.5	104	11.2	11.2	125	10.1	10.4	59	9.9	9.9	71	11.1	12.4
147	10.5	10.5	118	12.4	13	133	11.5	11.5	73	10.7	10.8	99	10.2	10.2
167	11.9	11.9	119	9.7	9.7	142	7.9	7.8	127	>14.0	>14.0	123	12.8	13
			133	11.8	11.8	156	11	11	142	11.1	11.1	127	11.2	11.2
			135	11	11	162	11.3	11.3	181	11.2	11.2	130	11.3	11.3
			140	11	11	166	10.8	10.7				132	9.5	9.5
			162	11.8	11.9	167	8.2	8.2				134	8.0	8
			164	9.8	9.8	171	11.2	11.3				141	11.0	11
												142	11.0	11
												152	8.6	8.7
												159	13.5	13.5
												167	11.0	11

means residue number; Mg (+) and Mg (–) mean whether an Mg^{2+} ion is present or not.

Comparison of the Results of MD Simulations with Experimental Data

To check the consistency between the simulations and the experiments, root mean square deviations (RMSD) of the results of the Mg^{2+}-bound GNBPs from their X-ray crystallographic structure counterparts were calculated. Table 6.2 shows that the RMSDs of all GNBPs were 1.2 Å on average and the standard deviations were small, which indicates that the structures obtained from the simulations were stable and compatible with the corresponding crystallographic structures.

In addition to RMSDs, B-factors of the Mg^{2+}-bound GNBPs were calculated and compared with the temperature factors of the respective X-ray crystallographic structures in order to examine whether our simulations reproduced the atom fluctuation in the experiment. Table 6.3 shows the sample cross correlations between the calculated B-factors and the experimental temperature factors. Although the B-factors and the temperature factors do not match perfectly due to the difference in the experimental and the computational conditions, the data indicate that the computational results have positive correlations with the experimental temperature factors (Table 6.3). These results demonstrate the success of MD simulations in reproducing the characteristics of the GNBPs' dynamics.

Table 6.2 RMSDs of the Mg^{2+}-bound GNBPs from the crystallographic structure

	H-Ras	RhoA	Rab6	Arf1	Ran
pK_a-PDB	1.15 ± 0.05	1.29 ± 0.11	1.17 ± 0.07	1.47 ± 0.24	1.20 ± 0.08
default-PDB	1.26 ± 0.09	0.90 ± 0.08	1.35 ± 0.11	1.33 ± 0.08	1.19 ± 0.06

Unit is Å. 750 sets of coordinates for the last 1.5 ns simulation (acquired every 2 ps) were used for statistics. pK_a-PDB represents the sample cross correlation values between the B-factors in the pK_a-determined protonation state and the experimental temperature factors. The default-PDB represents the values between the B-factors in the default protonation state of AMBER and the experimental ones.

Table 6.3 Correlations between B-factors and temperature factors of Mg^{2+}-bound GNBPs

	H-Ras	RhoA	Rab6	Arf1	Ran
pK_a-PDB	0.61	0.60	0.60	0.48	0.70
default-PDB	0.68	0.67	0.53	0.58	0.78

The last 1.5 ns simulation (acquired every 2 ps), 750 sets of coordinates, was used for statistics.

B-factors of GNBPs

To investigate which residues fluctuated, B-factors were calculated for every residue (Figure 6.2). The B-factors of Mg^{2+}-free H-Ras are largely different from those of Mg^{2+}-bound H-Ras, prominently in the switch 1 region (the residue number of 25-40) (Figure 6.2 (a)). In particular, Asp33 has the largest B-factor value in the Mg^{2+}-free form, which was approximately five times larger than that in the Mg^{2+}-bound form. Tyr32 to Tyr40 also largely fluctuated in the Mg^{2+}-free form. In the Mg^{2+}-bound form, the switch 2 region shows the largest B-factor, which was consistent with the crystallographic data.[146] This result also demonstrates the accuracy of the current MD simulations. The B-factors of RhoA in the Mg^{2+}-free form are larger than those in the Mg^{2+}-bound one from the switch 1 to the start of the switch 2 (the residue number of 27-63) (Figure 6.2 (b)). As for Rab6, the switch 1 (the residue number of 33-48) also has large B-factor values in the Mg^{2+}-free form. These results indicate that the absence of Mg^{2+} ions caused large fluctuations around the switch 1 of H-Ras, RhoA, and Rab6. However, the B-factors of Arf1 and Ran are different (Figure 6.2 (d) and 6.2 (e)). Both Mg^{2+}-free GNBPs show larger fluctuations in the regions between the switch 1 and the switch 2 regions (the residue number of 55-61 in Arf1, 49-58 in Ran). In addition, there are high peaks around the end of switch 2 (the residue number of 55-61 and the residue number of 130-140). At the C-terminus (the residue number of 187-215) of Mg^{2+}-free Ran, a high peak was also detected.

Figure 6.2 also shows the B-factors calculated with the AMBER default ionization state. It should be noted that the profiles of the B-factors of H-Ras and Rab6 are similar to the results in the pK_a-determined protonation state in that the B-factors at the switch 1 are large. As for RhoA, no prominent difference is observed between the Mg^{2+}-bound and the Mg^{2+}-free forms. Mg^{2+}-free Arf1 has larger values at switch 1 and the switch 2 regions, compared with the Mg^{2+}-bound form. In Mg^{2+}-free Ran, there are high peaks at the residue 130-140 and at the C-terminus, which resembles the result of Ran in the pK_a-determined protonation state. These results demonstrate that the switch regions are very sensitive to the Mg^{2+} ion removal.

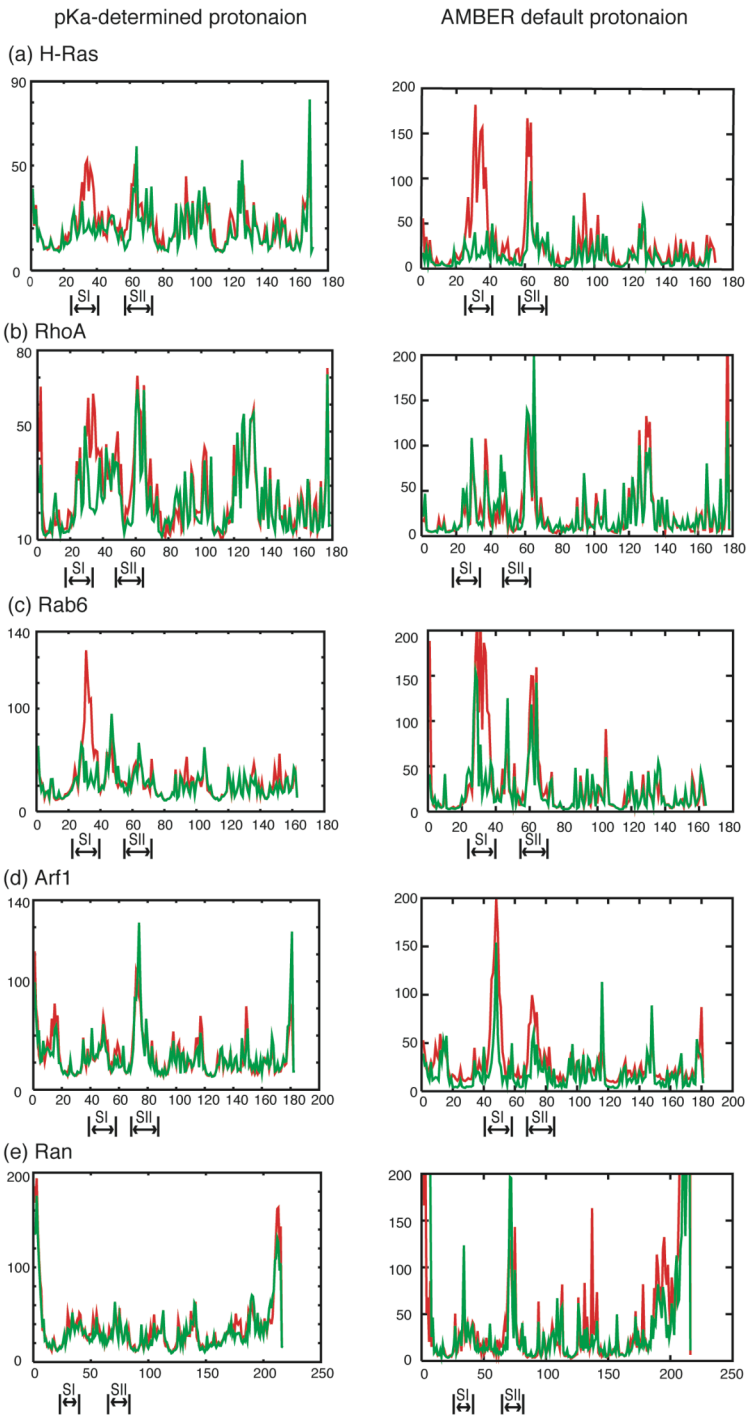

Figure 6.2 B-factors of Mg^{2+}-bound and Mg^{2+}-free forms

The abscissa represents the residue number. The green line represents the Mg^{2+}-bound form and the red line represents the Mg^{2+}-free form. SI and SII denote the switch 1 and the switch 2 regions. 750 sets of coordinates for the last 1.5 ns simulation (acquired every 2 ps) were used for calculation. Unit of B-factor is $Å^2$.

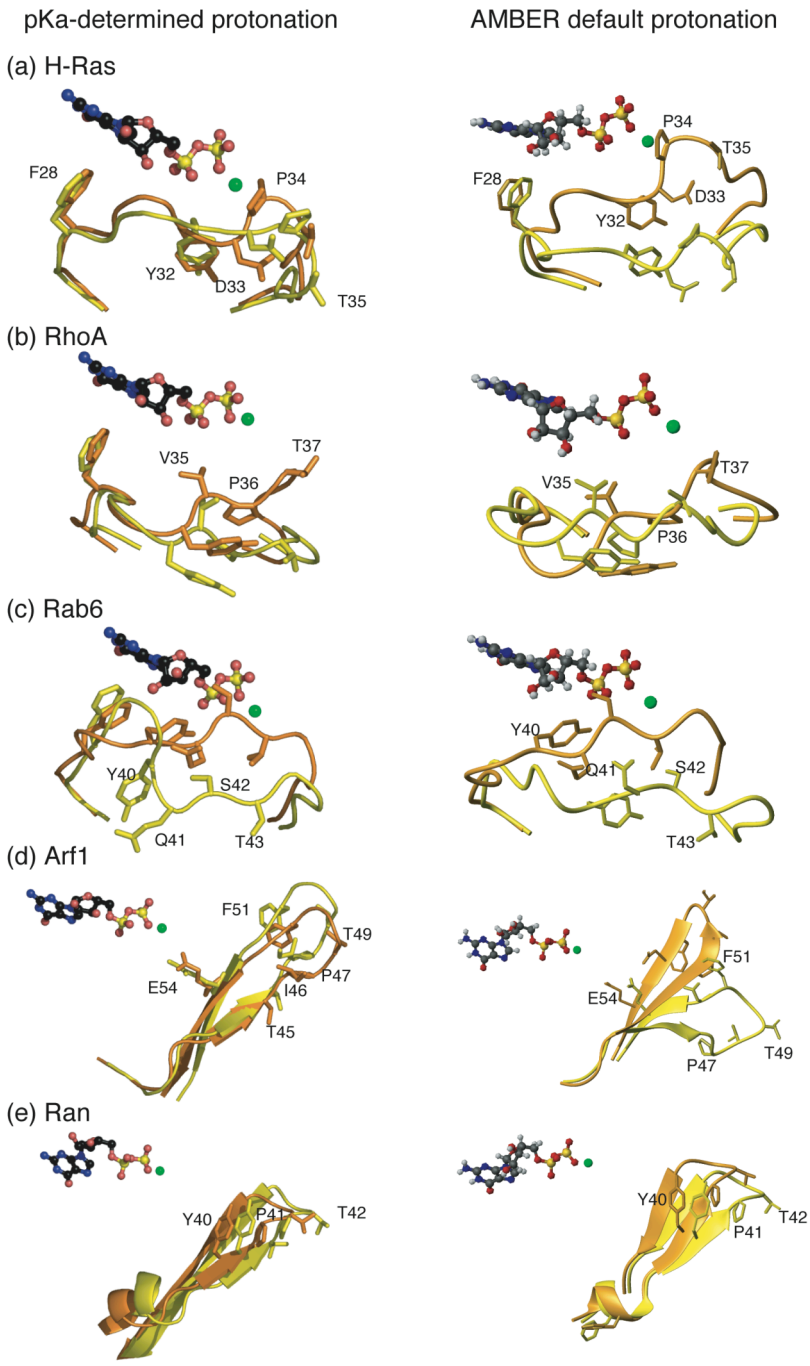

Figure 6.3 Switch 1 regions of Mg^{2+}-bound and Mg^{2+}–free forms

The Mg^{2+}-free and –bound forms are drawn in yellow and orange, respectively. (a) H-Ras (residues 25-40) (b) RhoA (residues 27-42) (c) Rab6 (residues 33-48) (d) Arf1 (residues 39-56) (e) Ran (residues 32-47)

Table 6.4 Distances between GDP-Pβ atom and Cα carbon atoms in Switch 1

		Y	X	P	T
H-Ras	Mg (+)	6.2 ± 0.3	6.7 ± 0.3	7.4 ± 0.6	10.5 ± 0.5
	Mg (–)	6.8 ± 0.5	8.7 ± 0.4	10.9 ± 0.5	13.6 ± 0.4
RhoA	Mg (+)	10.7 ± 0.4	8.2 ± 0.6	6.6 ± 0.4	6.6 ± 0.2
	Mg (–)	12.4 ± 0.5	12.4 ± 0.9	11.2 ± 0.8	12.8 ± 1.0
Rab6	Mg (+)	10.6 ± 0.4	7.4 ± 0.3	8.1 ± 0.4	5.6 ± 0.4
	Mg (–)	11.2 ± 0.5	12.7 ± 0.7	11.1 ± 1.1	9.7 ± 1.2
Arf1	Mg (+)	14.4 ± 0.4	18.9 ± 0.5	20.7 ± 0.4	18.5 ± 0.6
	Mg (–)	14.4 ± 0.4	19.1 ± 0.4	21.3 ± 0.4	18.8 ± 0.5
Ran	Mg (+)	18.5 ± 0.3	16.8 ± 0.3	18.5 ± 0.6	19.6 ± 0.4
	Mg (–)	19.6 ± 0.4	18.2 ± 0.5	20.1 ± 0.8	21.1 ± 0.5

The unit is Å. 500 sets of coordinates for the last 1 ns simulation (acquired every 2 ps) were used for statistics. YXPT stands for Tyr32, Asp33, Pro34, and Thr35 in H-Ras; Tyr30, Val35, Pro36, and Thr37 in RhoA; Tyr40, Gln41, Ser42, and Thr43 in Rab6; Thr45, Ile46, Pro47, and Thr48 in Arf1; Tyr39, Val40, Pro41, and Thr42 in Ran, respectively. Mg (+) and Mg (–) mean whether Mg^{2+} ion is present or not.

Conformations of Switch 1

Figure 6.3 and Table 6.4 show the computational results on the switch 1 conformations of the Mg^{2+}-bound and -free GNBPs. The switch 1 region of the Mg^{2+}-free H-Ras moves outside to detach from the GDP binding site, compared to the Mg^{2+}-bound form. In particular, Pro34 and Thr35, the last two residues of the YXPT motif, largely shift outward with no less than 3-4 Å and no longer participate in the nucleotide recognition. Moreover, the first two residues, Tyr32 and Asp33, also move from the original site. Phe28, which recognizes the guanine base of the GDP, do not change its location. In the case of the AMBER default protonation state, the conformational changes are exaggerated. The deviations of Pro34 and Thr35 were 6-11 Å, accompanied by a large movement of Tyr32 and Asp33. These results suggest that the removal of Mg^{2+} ion from H-Ras induces the conformational rebuilding of the switch 1 region, especially at the YXPT motif.

In the case of RhoA, the conformation at the switch 1 region in the Mg^{2+}-free form is prominently distinct from that of the Mg^{2+}-bound form (Figure 6.3 (b)). In the Mg^{2+}-free form, Thr37 (Thr35 in H-Ras), one of the ligands coordinated to the Mg^{2+} ion in RhoA, moves outside by approximately 6 Å compared with Mg^{2+}-bound form (Table 6.4). During the MD simulation, Pro36 began to move after Thr37 shifted, and became distant from the Mg^{2+}-binding site by 4.5 Å. The distances from the other two residues to GDP in Mg^{2+}-free RhoA are larger than the Mg^{2+}-bound form. Therefore, the switch

1 region becomes more distant from GDP in the Mg^{2+}-free form. A similar result was obtained when the AMBER default protonation state was used (Figure 6.3 (b)). These results indicate that the removal of Mg^{2+} ion had a remarkable influence on the conformation of switch 1 in RhoA, too.

The switch 1 region of Mg^{2+}-free Rab6 shows the largest conformational changes among all of GNBPs (Figure 6.3 (c) and Table 6.4). In the Mg^{2+}-free form, the distance between Thr43 (Thr35 in H-Ras) and the Mg^{2+}-binding site results in 9.7 Å, while the Mg^{2+}-bound form kept its distance with Thr35 at 5.5 Å during the simulation. Moreover, Tyr40, Gln41, and Ser42 (Tyr32, Asp33, and Pro34 in H-Ras) moved 0.8 Å, 5.3 Å, and 3.0 Å away from the nucleotide-binding site in the absence of Mg^{2+} ion. Like H-Ras, exaggerated results are obtained in the AMBER default protonation state. These results revealed that the Mg^{2+} ion played a key role to keep switch 1 closed in Rab6, similar to H-Ras.

When Mg^{2+}-bound and -free Arf1 were calculated with the pK_a-determined protonation state, they did not exhibit any obvious conformational changes in the switch 1 region (Table 6.4 and Figure 6.3 (d)). In contrast, when the AMBER default state was used, the most prominent conformational change in all GNBPs was observed in Mg^{2+}-free Arf1. Phe51, which was reported as a critical residue for the interaction with Gea2 (a GEF of Arf1),[136] is disclosed from the interior of the protein and is exposed to solvent in the Mg^{2+}-free form. In addition, the β-sheet in the switch 1 region of Arf1 is shortened by the absence of Mg^{2+} ion and changes its conformation to a loop shape. This result is consistent with the report indicating that the switch 1 region in the Arf1-Gea2 complex was completely a loop structure.[136] The large conformational difference is derived from a hinge motion at Thr43 and Thr44 (Tyr32 in H-Ras), which is located at the N-terminus of the YXPT motif (TIPT in Arf1; the residue number: 44-47) of switch 1. The torsion angles of Thr43 and Thr44 (ϕ, φ) = (-139.9º, 135.1º) in the Mg^{2+}-bound form changed to (ϕ, φ) = (-69.7º, 153.6º) in the Mg^{2+}-free form.

As for Ran, the secondary structure of the GDP-Mg^{2+}-bound form in the crystal structure was quite similar to Arf1, where they have a seventh β–strand and the switch 1 consists of β–sheet. Interestingly, the current computational results reveals that the conformational change of the switch 1 region is compatible between Ran and Arf1; that is, Mg^{2+}-free Ran barely deviated from the Mg^{2+}-bound form (Figures 6.3 (e)). There is only a small displacement in switch 1, where it slightly moves away from the Mg^{2+}-binding site due to the conversion from the Mg^{2+}-bound to the Mg^{2+}-free form.

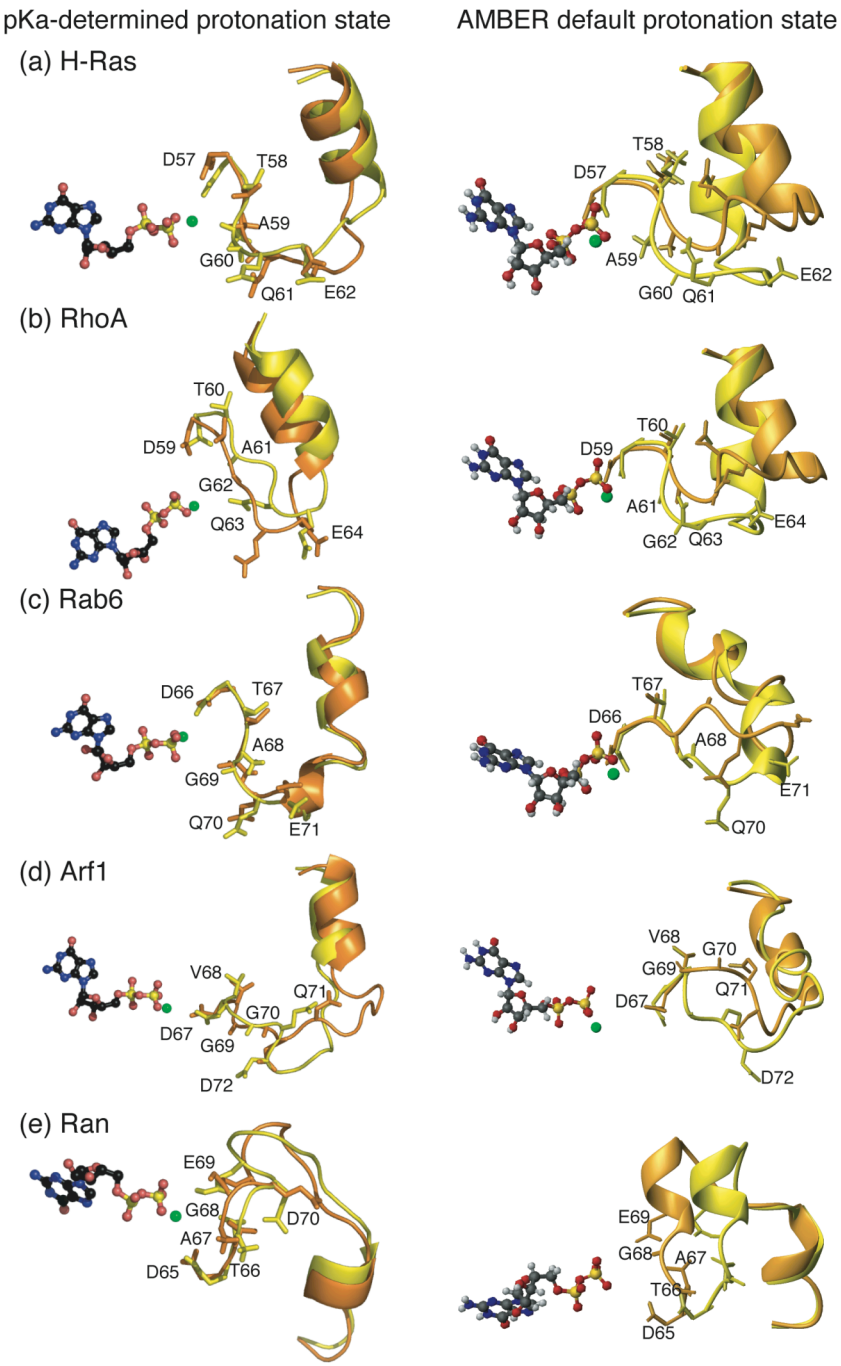

Figure 6.4 Switch 2 regions of Mg^{2+}-free and Mg^{2+}–bound forms.

Coloring method is same as Figure 6.3. (a) H-Ras (residues 57-75) (b) RhoA (residues 59-77) (c) Rab6 (residues 66-84) (d) Arf1 (residues 67-85) (e) Ran (residues 65-83).

Table 6.5 Distances between GDP-Pβ and backbone carbonyl oxygen atoms of Switch 2

		D	T	A	G
H-Ras	Mg (+)	7.94 ± 0.27	5.67 ± 0.19	8.19 ± 0.42	10.31 ± 0.36
	Mg (–)	9.75 ± 0.26	7.19 ± 0.36	6.89 ± 0.80	10.80 ± 0.37
RhoA	Mg (+)	9.88 ± 0.23	5.71 ± 0.20	8.88 ± 0.31	10.13 ± 0.50
	Mg (–)	10.68 ± 1.04	9.22 ± 0.80	11.36 ± 0.77	12.52 ± 1.04
Rab6	Mg (+)	10.63 ± 0.22	6.02 ± 0.19	5.87 ± 0.41	8.14 ± 0.26
	Mg (–)	9.03 ± 0.30	6.18 ± 0.43	8.13 ± 0.52	8.26 ± 0.36
Arf1	Mg (+)	9.65 ± 0.21	9.57 ± 0.29	14.08 ± 0.46	16.45 ± 0.72
	Mg (–)	9.73 ± 0.21	10.43 ± 0.23	14.22 ± 0.33	17.55 ± 0.40
Ran	Mg (+)	9.51 ± 0.25	7.04 ± 0.22	8.91 ± 0.73	9.04 ± 0.60
	Mg (–)	10.78 ± 0.41	8.02 ± 0.42	10.40 ± 0.64	10.38 ± 0.44

The unit is Å. 500 sets of coordinates for the last 1 ns simulation (acquired every 2 ps) were used for statistics. DTAG means Asp57, Thr58, Ala59, and Gly60 in H-Ras; Asp59, Thr60, Ala61, and Gly62 in RhoA; Asp66, Thr67, Ala68, and Gly69 in Rab6; Asp67, Val68, Gly69, and Gly70 in Arf1; Asp65, Thr66, Ala67, and Gly68 in Ran respectively. Mg (+) and Mg (–) mean whether a Mg^{2+} ion is present or not.

Conformations of Switch 2

The switch 2 regions in the Mg^{2+}-bound and -free H-Ras had a prominent difference at the DTAG motif and its adjacent regions containing a loop and an α-helix (Figure 6.4 (a)). Ala59 approached the Mg^{2+}-binding site (Table 6.5), which is consistent with the X-ray crystallographic structure of the H-Ras-SOS complex.[135] Asp57 and Thr58, which formed H-bonds with water molecules and stabilized the coordination of Mg^{2+} ion via these water molecules in the Mg^{2+}-bound form, detached themselves from GDP (Table 6.5) and altered their torsion angles (Δφ was 50º and –30º, respectively) in the Mg^{2+}-free form. It was also found that these changes of Asp57 and Thr58 preceded the movement of Ala59. Hence, these two residues, which are located at the hinge of the switch 2 in H-Ras, induce the movement of Ala59.

The switch 2 in RhoA has the largest conformational change in all of GNBPs (Figure 6.4 (b)). All of the four residues in the DTAG motif shift away from GDP (Table 6.5). Asp59 and Thr60 (Asp57 and Thr58 in H-Ras) exhibit large torsion changes similar to H-Ras, while Ala61 (Ala59 in H-Ras) departs from the Mg^{2+}-binding site in contrast to H-Ras.

In the case of Rab6 in the Mg^{2+}-free form, the switch 2 shows some conformational changes, but scarcely moves from the initial position (Figure 6.4 (c)). Asp66 (Asp57 in H-Ras) approaches toward GDP by 1.6 Å (Table 6.5), and Ala68 (Ala59 in H-Ras)

moves away from GDP by 2.3 Å. As a result, switch 2 was kept at the original position.

As for Mg^{2+}-free Arf1 and Ran, the residues at the DTAG motifs detached slightly from GDP (Figures 6.4 (d) and (e)). The switch 2 region shifted away from the Mg^{2+}-binding site by approximately 0.6 Å and 1.3 Å in Mg^{2+}-free Arf1 and Ran, respectively. However, these changes were relatively small compared with H-Ras, RhoA.

In all GNBPs, the conformational changes of the switch 2 were exaggerated when the AMBER default protonation state was used (Figure 6.4), which is similar to the results of the switch 1 region.

Overall Structural Changes from the Viewpoint of Molecular Surface and Solvent Accessible Surface Areas

GNBPs' molecular surfaces and solvent accessible surface areas (SASA) after the simulations are shown in Figure 6.5 and Table 6.6, respectively. Due to the large conformational changes of the switch 1 region (Figure 6.3 (a)), the whole structure of H-Ras had a groove between the switch 1 and the GDP binding site in the Mg^{2+}-free form (Figure 6.5 (a)). Furthermore, in the AMBER default protonation state, a larger groove is also created around the GDP binding site, which doubled the SASA of GDP in the absence of Mg^{2+} ion.

Similarly, the removal of Mg^{2+} ion from RhoA created a groove between the C-terminus of the switch 1 region and the midst of the switch 2 region (Figure 6.5 (b)). The SASA increased by 309 $Å^2$ as a result of the formation of the groove. In contrast, any groove cannot be observed in the case of using the AMBER default protonation state, and the SASA decreased.

In Rab6, on the other hand, the absence of the Mg^{2+} ion created a groove between the GDP binding site and the switch 1 region (Figure 6.5 (c)). The conserved motif regions of P-loop, switch 1 and 2, NKXD, and SAK surrounded this groove. A similar groove was observed in the calculation with the AMBER default protonation state. According to the creation of the grooves, the SASAs of Mg^{2+}-free Rab6 increased by 274 $Å^2$ and 419 $Å^2$ in the pK_a-determined and the AMBER default protonation states, respectively.

Such a groove was also found in Mg^{2+}-free Arf1, which was not obvious in the pK_a -determined protonation state while clearly observed in the AMBER default state (Figure 6.5 (d)). Although there was little difference in the conformation between the Mg^{2+}-bound and the Mg^{2+}-free forms in the pK_a-determined protonation state, the

SASA increased by 190 Å^2. The changes of the SASA around the switch 1 and the switch 2 regions contributed to this increase of the SASA. In the AMBER default protonation state, it should be noted that the SASA increased by no less than 800 Å^2. This increase of the SASA mainly attributes to the switch 1 conversion from the β-sheet conformation to the loop in the absence of the Mg^{2+} ion. In particular, exposure of Phe51 to the solvent contributed to the increase of the SASA (the SASA of Phe51 changed from 45.5 to 157.5 Å^2). The motion of Phe51 was fundamentally due to the structural change in the switch 1 region.

In the case of Ran, no clear groove was seen in the Mg^{2+}-bound and -free forms in the pK_a-determined protonation state, while the creation of a groove was observed in the AMBER default protonation state (Figure 6.5 (e)). Despite the absence of the groove in the former case, the SASA increased by 327 Å^2, which was similar to the case of Arf1 as described above. In the AMBER default protonation state, the Mg^{2+}-free Ran made a groove between the NBD region and the switch 2 region, while other GNBPs exhibited the conformational change mainly at the switch 1 regions. As a result, the SASA increased by 241 Å^2.

Table 6.6 Solvent accessible surface areas of GNBPs.

	H-Ras	RhoA	Rab6	Arf1	Ran
Mg(+)*	8269	9862	8406	9655	11195
Mg(−)*	8633	10171	8680	9845	11522
ΔSASA	364	309	274	190	327
Mg(+)**	8686	9887	8379	9191	11602
Mg(−)**	8918	9765	8798	9993	11843
ΔSASA	232	-122	419	802	241

The unit is Å^2. Mg (+) and Mg (−) mean whether an Mg^{2+} ion is present or not. * means the values calculated with the AMBER default protonation state. ** means the values calculated with the p*Ka*-determined protonation state

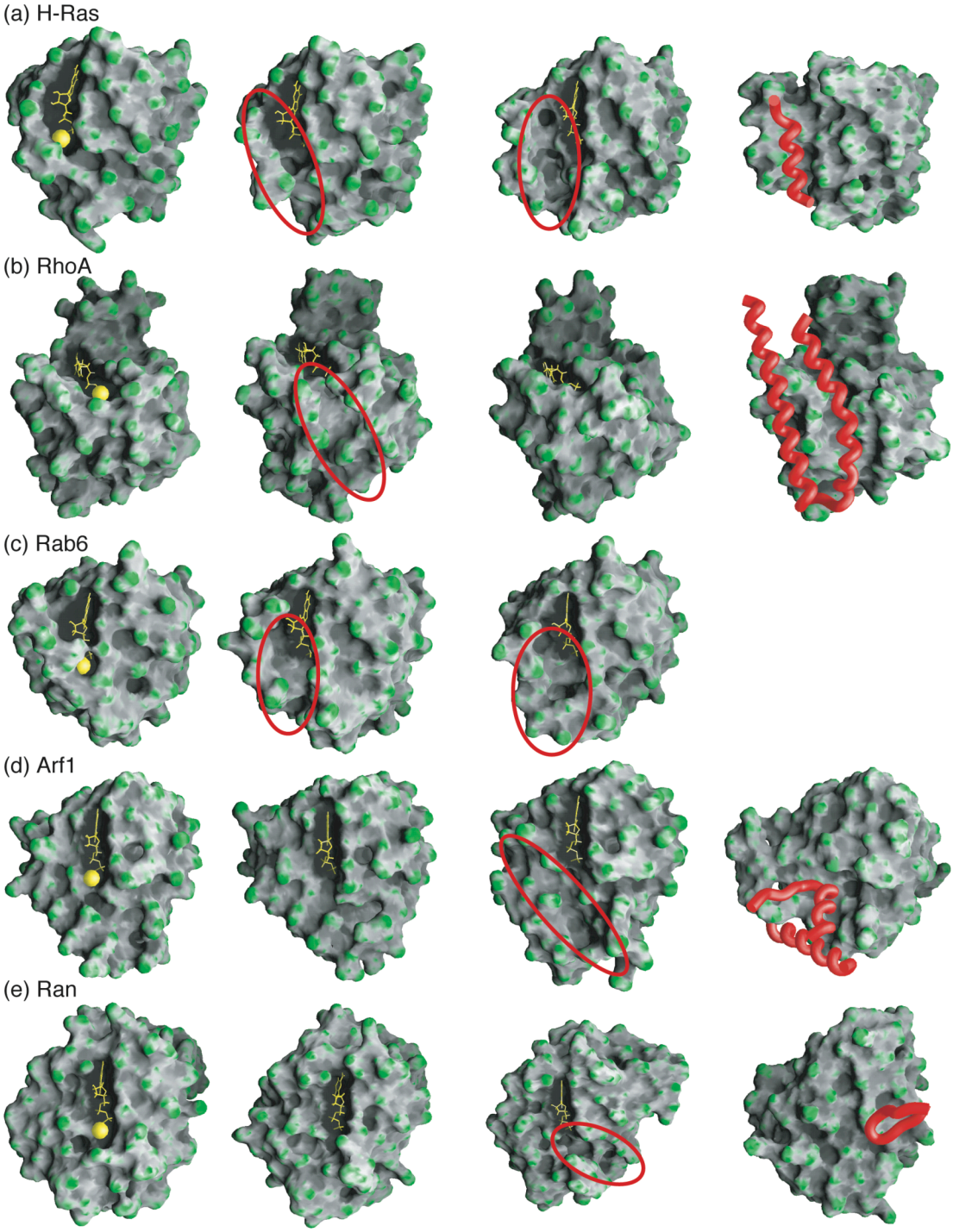

Figure 6.5. Molecular surfaces of Mg^{2+}-bound and Mg^{2+}-free forms.

The Mg2+-bound form is in the left column; the Mg^{2+}-free form (pKa-determined protonation state) in the middle-left; the Mg^{2+}-free form (AMBER default protonation state) in the middle-right; the GEF-bound form obtained experimentally in the right,. The GEF-bound form for Rab6 is unavailable. GDPs and Mg^{2+} ions are represented by the sticks and the spheres colored yellow. The helices or loops of GEFs interacting with GNBPs are represented as red tubes. Red circles indicate the grooves appearing due to the absence of the Mg^{2+} ion. These structures are the final 0.2 ns averages of the MD simulations.

VI.4 Discussions

We calculated Mg^{2+}-bound and Mg^{2+}-free H-Ras, RhoA, Rab6, Arf1, and Ran proteins and compared their conformations to reveal the role of the Mg^{2+} ion in regulating GNBPs' structures. The results show that the lack of the Mg^{2+} ion induces large conformational changes in the switch regions. Although the switch regions intrinsically have dynamic properties, the results demonstrate that the lack of Mg^{2+} ion enhances the mobility of the switch regions (Figure 6.2). Due to the flexibility, large conformational changes occurred around the GDP binding sites (Figures 6.3, 6.4). The Mg^{2+}-bound and -free GNBPs were also calculated under the default protonation state of AMBER at pH 7.0. The results shows that the AMBER default protonation state exaggerates the fluctuation and the conformational changes in the absence of the Mg^{2+} ion (Figure 6.2, 6.3, 6.4). Switch 1 and 2 fluctuated much more than the other regions, which resulted in producing distinct differences between the Mg^{2+}-bound and -free forms. The characteristic grooves are also observed in Arf1 and Ran (Figure 6.5). This demonstrates that the conformational changes are very sensitive to the protonation state of the amino acid residues.

To investigate the cause for the switch motion, H-Ras was chosen as a representative of the GNBPs, and the quantum chemical calculation was performed using the FMO (fragment molecular orbital) method. The fundamental concept of the FMO method is to divide the protein into the fragments consisting of one or two residues, which enables the quantum chemical calculation of the whole part of the protein.[155] The FMO calculation revealed the existence of a large repulsive energy between the switch regions and GDP (Figure 6.6). This result suggests that the repulsion energy between the switch region and GDP would force the switch region to move away from the GDP-binding site. Because of the positive charge of the Mg^{2+} ion and its interaction with the main chain or the side chain atoms in the switch regions, the Mg^{2+} ion buffered these repulsive interactions in the Mg^{2+}-bound form. Accordingly, the removal of the Mg^{2+} ion increased the fluctuation of the switch regions in the current MD simulations.

The computational results can be compared with the experimental structures for the GNBPs complexed with the respective GEFs, in which the GNBPs have neither Mg^{2+} ion nor GDP. Moreover, they exhibit large conformational changes in the switch regions. Solvent accessible surfaces of the Mg^{2+}-bound, the Mg^{2+}-free, and the GEF-bound GNBPs are shown in Figure 6.7. In H-Ras, our calculations indicate that the absence of Mg^{2+} ion makes a groove between the nucleotide-binding domain and the switch 1 region (Figure 6.5 (a)). It should be noted that such a groove is also found in H-Ras bound to the Cdc25 domain of Son of sevenless (SOS) (Ras-GEF),[135] in which there is no Mg^{2+}

ion; moreover, a conformational change appeared in the switch 1 region (Figure 6.7 (a)). A striking similarity between the two structures is the switch 1 regions located apart from the nucleotide-binding site. These conformations require for H-Ras to accommodate the α-helix of SOS in order to make a complex. The transformation of the pocket into the open form induced by SOS increases the solvent accessible surface areas around the nucleotide-binding site consisting of the conserved motif regions (P-loop, switch 1 and 2, NKXD, and SAK). This increase was also observed in the MD simulations. The superposition of the structure of Mg^{2+}-free H-Ras on the SOS-bound form gives the root-mean-square deviation (RMSD) value of 2.0 Å. On the other hand, the RMSD is 3.0 Å between Mg^{2+}-bound and SOS-bound H-Ras. These results indicate that the lack of Mg^{2+} ion induces H-Ras to resemble SOS-bound forms, especially in the switch 1 region.

As for Mg^{2+}-free RhoA, the groove appearing in the absence of Mg^{2+} ion is located between the C-terminus of the switch 1 and the switch 2 whichever the default or the pKa-determined protonation state is used (Figure 6.7 (b)). Surprisingly, the binding site of Dbl (Rho-GEF) is also the same position, at which Dbl interacts with RhoA through its α–helix.[138]

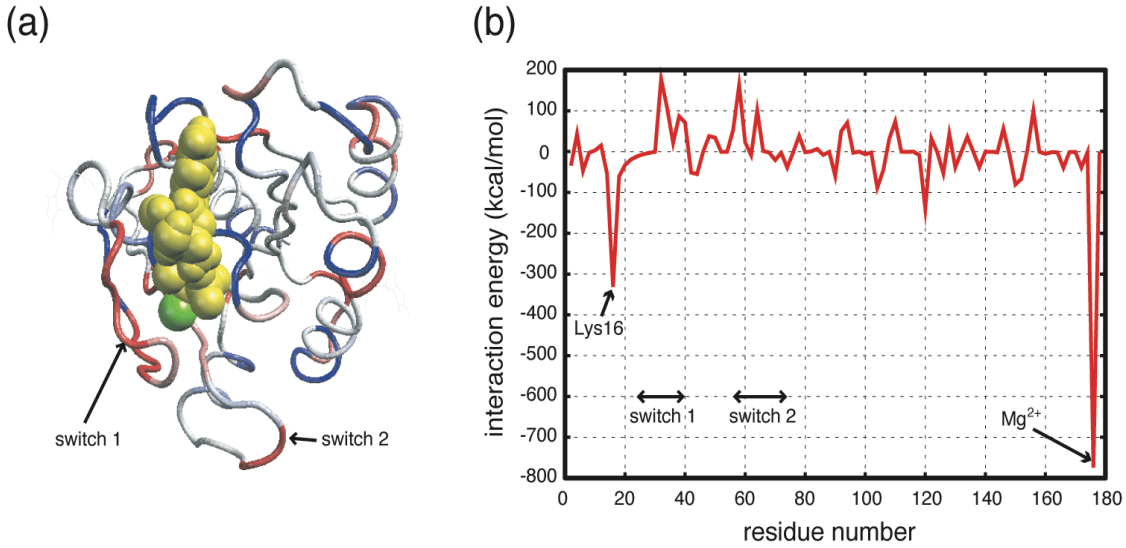

Figure 6.6 Interaction energy between GDP and the other residues of H-Ras

The interaction energy was calculated by the fragment molecular orbital (FMO) method with the STO-3G basis set, calculated with the AMBER default protonation state. (a) The whole structure of the H-Ras protein. The residues with the negative interaction energy for GDP are colored by blue, and those with the positive one are colored by red. GDP and Mg^{2+} ion are represented by the yellow and the green spheres, respectively. (b) Plot of the interaction energy. The abscissa represents the residue number.

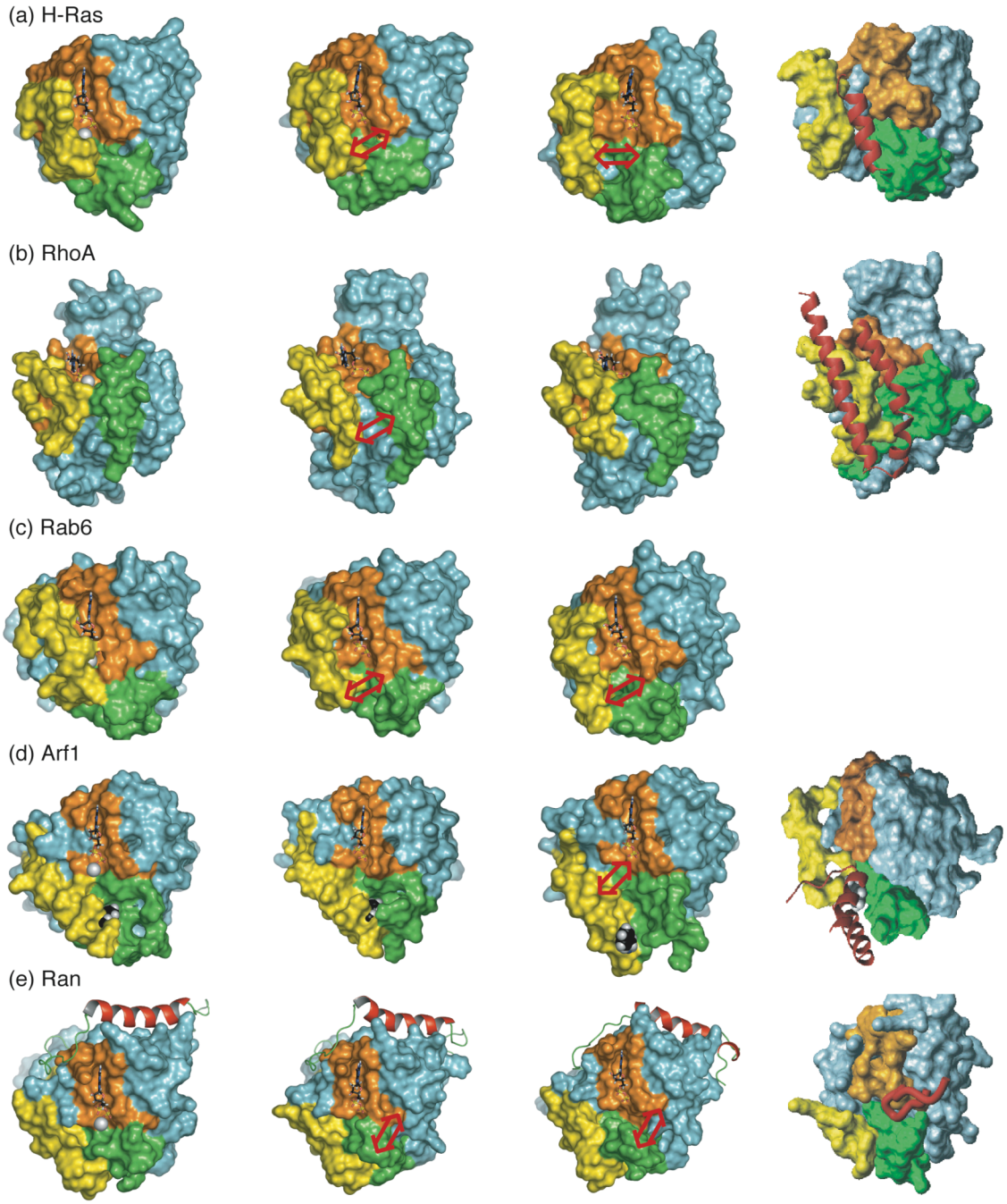

Figure 6.7 Solvent accessible surfaces of Mg^{2+}-bound, Mg^{2+}-free, and GEF-bound forms.

The Mg^{2+}-bound form in the left column; the Mg^{2+}-free form (p*Ka*-determined protonation state) in the middle-left; the Mg^{2+}-free form (AMBER default protonation state) in the middle-right; the GEF-bound form in the right. GDPs are shown as a ball-and-stick representation. White spheres represent Mg^{2+} ions. The switch 1, the switch 2, and nucleotide-binding regions are colored with yellow, green, and dark orange, respectively. The rest is sky blue. Red tubes represent the helices or loops of GEFs. Red arrows indicate the grooves appearing due to the absence of Mg^{2+} ion. These time-average structures were obtained from the final 0.2 ns MD simulations.

In the case of Ran and Arf1, the switch regions move slightly away from the GDP binding sites (Figure 6.7 (d) and (e)). In the case of the AMBER default protonation state, the grooves are clearly observed in these proteins in the Mg^{2+}-free forms. In the case of Ran, similar to H-Ras and RhoA, the position of the groove is identical with that of Ran-RCC1 (Ran-GEF) interaction site, into which RCC1 inserts a loop (Figure 6.7 (e)). Unfortunately, the C-terminal region of Ran cannot be compared with RCC1-bound Ran because the mobility of the region was too large to be observed experimentally in the RCC1-bound state.[137] In the absence of Mg^{2+} ion, Arf1 exhibits large conformational changes in the switch 1 region, which induces the deformation in some parts of the seventh β-sheet, which makes Phe51 expose to surface from inside of Arf1 (Figure 6.7 (d)). Interestingly, the conversion of the switch 1 region into a loop conformation and the exposure of Phe51 are also found in the Arf1-Gea2 complex[136] (Gea2 is one of the Arf1's GEFs) (Figure 6.7 (d)). The switch 1 completely forms a loop in the Arf1-Gea2 complex. The switch 1 of Mg^{2+}-free Arf1 in simulation is partially in a loop conformation while that of Mg^{2+}-bound state remains in a β-sheet conformation. It should be noted that the mutation of Phe51 was reported to be critical for GEF-binding.[136] Although Rab6 exhibited the conformational changes similar to H-Ras, it cannot be compared with a GEF-bound form, because the X-ray crystallographic structure is not available. However, Rab6-GEF would interact with a groove between the switch 1 and the GDP binding site, similar to the H-Ras-SOS interaction. Judging from these findings on the structures of the Mg^{2+}-free GNBPs, the removal of Mg^{2+} ion is concluded to have a keen role to induce a large conformational change of GNBPs to prepare the template for GEF binding.

It is reported that the point mutation of H-RasS17N, which is critical for the Mg^{2+} coordination, caused an increase of GEFs' affinity.[156] In addition, the chelation of the Mg^{2+} ion increases the affinity of H-Ras for SOS and enhances the dissociation of GDP.[133,157] N-Ras, an isoform of H-Ras, has 10 times greater affinity for GTP than GDP at low Mg^{2+} concentrations, whereas the affinities of GTP and GDP are approximately the same at high Mg^{2+} concentrations.[140] Additionally, several mutational studies of other small G-proteins revealed the importance of the Mg^{2+} ion for the GEF binding. Rab3AT36N[158] and RanT24N[159] (analogous to H-RasS17N) mutants were pointed out that they had greater affinity for their respective GEFs than their wild-types. All mutated residues have been demonstrated to be essential to the coordination of the Mg^{2+} ion. In the Rho family, it was proposed that GEF had a negative correlation with the free Mg^{2+} ion in the cell; thus, high concentrations of Mg^{2+} ion decreased GEF affinity for GNBPs.[160] The role of the Mg^{2+} ion for GDP binding was supposed to stabilize the GDP-binding state, since the presence of the Mg^{2+} ion prevented GDP dissociation in various GNBPs;[160,161] moreover, the picomolar levels of the Al^{3+} ion competed with the Mg^{2+} ion and inhibited the GDP/GTP exchange of

Ras.[162] Furthermore, the crystallographic studies of GDI-bound GNBPs revealed that the GDIs inhibited GDP dissociation by stabilizing the Mg^{2+} binding.[163] All the experimental data mentioned above suggest that the lack of the Mg^{2+} ion increases the affinity for GEFs and promotes the GDP dissociation.

Formerly, GEFs were assumed to promote GDP dissociation by disrupting the Mg^{2+} coordination of GNBPs. But recently, some studies provided different viewpoints on the relationship between GEF and Mg^{2+} ion. A structure-based mutagenesis study of H-Ras and SOS (Ras-GEF) proteins demonstrated that mutations of the residues in SOS, which were expected to disrupt the Mg^{2+}-binding site, had no effect on the catalytic function of SOS.[164] Furthermore, a fluorescence study on Rac, a member of Rho family, demonstrated that the release of Mg^{2+} ion led to the GDP dissociation in its GDP/GTP exchange reaction.[145] These studies indicated that the disruption of Mg^{2+} coordination was independent of GEFs and that the exchange reactions were dominated by the binding of GEFs to the Mg^{2+}-free but nucleotide-bound GNBPs. That is, it can be speculated that the release of the Mg^{2+} ion induces the interaction of GEFs with GNBPs. The present results provide a new semiopen model that can be a template for GEF binding. Moreover, the current MD simulations have demonstrated that the absence of Mg^{2+} ion converts the conformation of not only RhoA but also all members of the small G-proteins to the semiopen forms. Consequently, Mg^{2+} ion regulates the conformations of the small G-proteins.

Mg^{2+} ions are universally present in a cell, and the concentration of the Mg^{2+} ion may locally change as Ca^{2+} ions do (due to various stimulations such as the elevation of cation, anion, and ATP concentrations in the cell). The concentration of the Mg^{2+} ion possibly determines what states a small G-protein is, whether at the closed form when the Mg^{2+} concentration is high or at the semiopen form when the Mg^{2+} concentration is low.

VI.5 Conclusion

Small G-proteins, H-Ras, RhoA, Rab6, Arf1, and Ran, can change their conformations dramatically responding to the surrounding ionic environment. Mg^{2+} ion, in particular, is critical for determining p*Ka* values of amino acid residues around the switch regions and their conformational changes. The removal of Mg^{2+} ion converts their conformations into semi-open form that can easily interact with the corresponding GEFs.

VII

MD Simulations of H-Ras protein on Membrane

Abstract

Farnesylated H-Ras at the membrane-water interface was calculated to investigate the effects on the structures of H-Ras and the interface. Two membranes described in *Chapter VI* were used as the biomembrane model. A developed method how the H-Ras approaches to and bound with lipid bilayers predicted a probable complex structure, where the lipid anchor of the H-Ras was located at the membrane-water interface and the GDP-binding site was away from the membrane. The conformation was caused due to the electrostatical repulsive forces working between the GDP-binding switch regions and the negative charges of the acidic lipids. Detailed analyses of these structures reveal the interactions of the farnesyl moiety with the surrounding lipid molecules.

VII.1 Introduction

Ras proteins have been studied intensively for more than a quarter century because of their role in human cancer.[46] Three members of the Ras family, H-Ras, N-Ras, and K-Ras, are expressed in mammalian cells, in which they are localized on distinct lipid microdomain.[165] An H-Ras protein is a representative of small G-protein family as described in the previous chapter. It exists as a lipid-anchored membrane protein in the cell. H-Ras is farnesylated at the 186 cystein and further added two palmitoyl moieties to the 181 and 184 cysteines. The addition and the removal of the palmitoyl groups is enzymatically controlled, which regulate the localization of H-Ras in the cell.[33] Moreover, H-Ras shows dual microlocalization dependent on its state. A GDP-loaded inactive H-Ras is localized in lipid raft, but a GTP-loaded active H-Ras is away from the raft and moves around non-raft, or more disordered regions.[166] The microlocalization mechanism of H-Ras has been intensively investigated for recent five years[167-170] after the concept of lipid raft was extensively accepted in the molecular biological field[23] (see the review article[171] written by Hancock and Parton for review).

The microlocalization of H-Ras is more complex than the other membrane proteins with a simple lipid anchor, because of its dual lipidation, palmitoylation and farnesylation. Although prenylated proteins have been reported to be largely excluded from lipid rafts, the combination of palmitoylation and farnesylation allows GDP-loaded H-Ras to access lipid rafts. However, the additional palmitoylation of GDP-loaded H-Ras is not enough to completely localize the protein to lipid rafts. Therefore, the protein exists in a dynamic equilibrium between the liquid-ordered and disordered plasma membranes. Even when H-Ras is activated, the protein still can accesses lipid rafts, although the equilibrium shifts in favor of residence in disordered regions.

In order to reveal the biophysical mechanism for the dynamical equilibrium of H-Ras, it is quite important to understand the interactions between H-Ras and lipid membranes. Therefore, MD simulations of the farnesylated H-Ras (Far-Ras) on the asymmetric membranes described in *Chapter IV* were carried out. The results allow us to observe the detailed interaction between the protein and lipids.

VII.2 Computational Details

Modeling Initial Structures

Figure 7.1 summarizes the procedure for modeling initial structures of H-Ras on asymmetric membranes.

At first, the structure of the C-terminus of H-Ras was predicted with MD simulations, because the X-ray crystallographic structure lacks 20 amino acid residues (residue number: 170-189). MD simulations were performed for 2 ns using AMBER[34] with the implicit water model implemented in Generalized-Born method and with no cut-off distance for calculating the non-bonded interactions.

Then, a farnesyl moiety was added to Cys186, and an additional 1 ns MD simulations was carried out for equilibration. The predicted structure of the farnesylated H-Ras is shown in Figure 7.1 (a). The molecular structure of farnesyl cystein (F-Cys) was constructed by the program *GaussView* and was optimized at the HF/3-21G level with SCRF method by Onsager model.[172] The electrostatic potential of F-Cys was calculated by Gaussian 98 at the B3LYP/6-31G** level. The atomic charges were generated by fitting them to the electrostatic potentials with the *RESP* module of AMBER.[34] The missing parameters were created based on the analogy with available parameters in AMBER parm99 force field parameters set.

Second, farnesylated H-Ras (Far-Ras) was put on the membrane (Figure 7.1 (b) - (f)). In order to predict the orientation of Far-Ras, potential energy calculations were performed using Delphi program for 144 structures generated by rotating the Far-Ras on the membrane at every 30 degrees horizontally and vertically (Figure 7.1 (b) and (c)). And then, the rotamer with the lowest energy was selected to perform a further calculation for approach of Far-Ras to the membrane (Figure 7.1 (d) and (e)). In these structures, the structure with the lowest energy was used for the initial structure for further MD simulations of H-Ras on the membranes (Figure 7.1 (f)).

Details of MD Simulations of Ras-membrane Complexes

MD simulations of Far-Ras-membrane complexes were performed using NAMD 2.6[69]. Charmm22[35] is used as the force field parameters for the protein. The other detailed procedure and parameters of MD simulations are the same as described in other chapters. MD simulations were performed for 6 ns. The last 2 ns data were used for analysis.

Insertion of the farnesyl group was carried out by imposing the force directed to the membrane's center on the terminal atom of the group. After the insertion, 1 ns extra equilibrium simulations were performed.

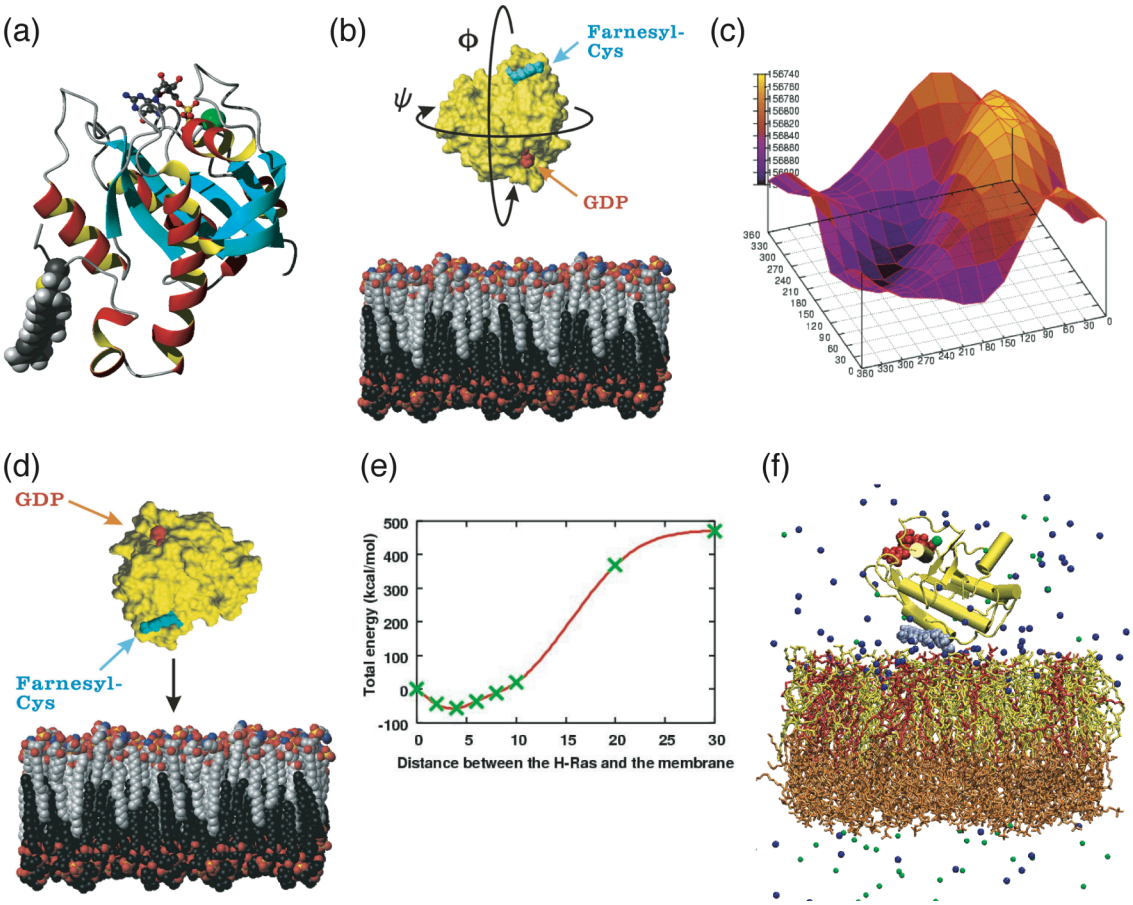

Figure 7.1 Methods for predicting a structure of Far-Ras on membrane.

(a) Schematic predicted structure of the farnesylated H-Ras (Far-Ras). GDP is represented as ball-and-stick model, and farnesyl-cystein and Mg ion is represented as van der Waals spheres. Mg ion is colored green (b) Schematic view of Far-Ras rotating on the membrane. (c) The three-dimensional plot of the potential energies calculated for the 144 rotamers generated by (b). (d) Schematic view of Far-Ras approaching the membrane. (e) The plot of the potential energies calculated for the structures generated by (d). (f) The predicted structure of Far-Ras on the membrane (blue and green spheres are Na^+ and Cl^- ions; orange, yellow, and red sticks are POPC, POPE, and POPS, respectively).

VII.3 Results and Discussion

Orientation of Farnesylated H-Ras on Membranes

The farnesylated H-Ras was located on the membrane with GDP-binding site away from the membrane surface resulted from the energy calculation (Figure 7.2). As a result, the farnesyl moiety is located on the membrane interface. This complex structure was stabilized by the positive charges of amino acids around the lipid anchor. Therefore, a delicate balance between the electrostatically attractive and repulsive forces is the main factor for determining the orientation of H-Ras on the membrane.

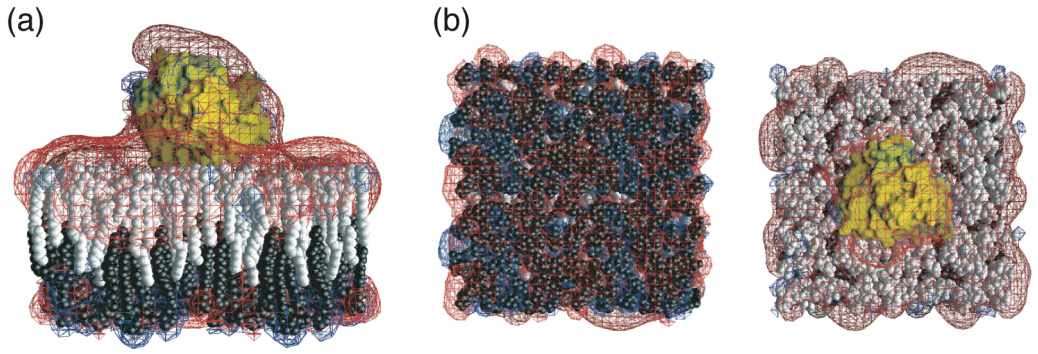

Figure 7.2 Electrostatic potential of H-Ras-membrane complex.

(a) Side view. (b) Top view (left, exoplasmic face; right, endoplasmic face). H-Ras is colored yellow. The exoplasmic and endoplasmic faces are represented as black and white van der Walls spheres. Red and blue meshes mean –25 mV and +25 mV iso-potential surfaces, respectively.

Interactions between H-Ras and Lipids

Figure 7.3 shows the distance between Far-Ras and the lipid bilayer. The distance kept 1 nm, which indicates that the Far-Ras was stably located on the membrane from the start to the end of simulation, and the attractive forces worked continuously. Detailed observation of the protein-lipid interface revealed the cause of the attraction. Figure 7.4 shows the protein-lipid interface and the interactions between them. The head groups of POPS and POPE formed H-bonds with amino acids of Far-Ras. In particular, POPS and Arg formed strong stable H-bonds (Figure 7.4 (b)). POPS molecules protruded from the membrane surface for the interaction with Far-Ras (Figure 7.4 (a)). These attractive interactions were also reflected on the correlation between the lateral diffusion of Far-Ras and POPS molecules (Figure 7.5). The co-lateral movement of Far-Ras and POPS is due to the strong attractive forces between them.

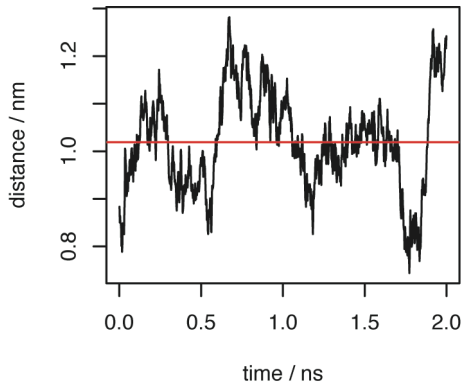

Figure 7.3 Distance between H-Ras and membrane.

Red line indicates the averaged distance.

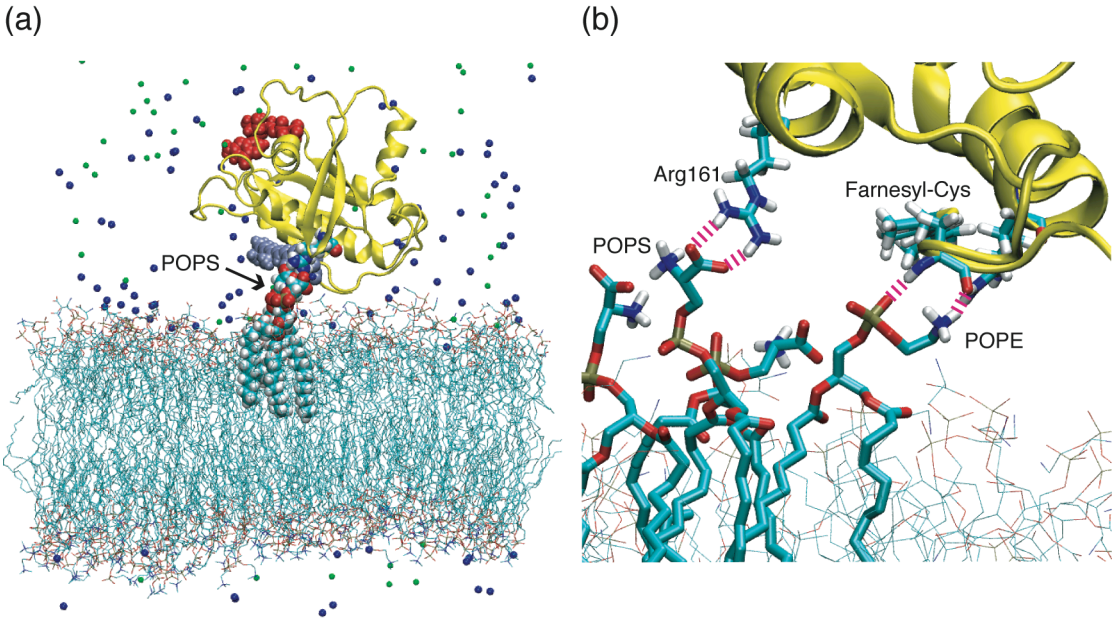

Figure 7.4 Interactions between H-Ras and lipids.

(a) Protrusion of POPS molecules from the membrane surface. (b) Detailed view of interactions between H-Ras and lipids. Arg161 and farnesyl-Cys residues, POPS and POPE molecules are represented by sticks colored by atom types (C, cyan; O, red; N, blue; H, white; S, yellow). The other part of H-Ras is colored yellow. The purple dashed lines indicate hydrogen bonds between H-Ras and lipids. Blue and green spheres are Na^+ and Cl^- ions.

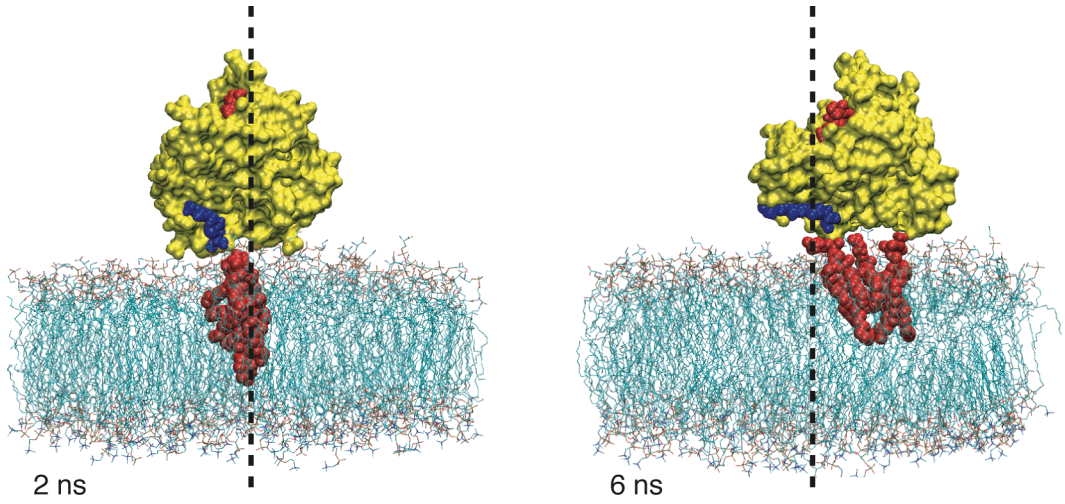

Figure 7.5 Correlation between lateral diffusion of H-Ras and POPS molecules.

Dashed lines are the centerlines through the system. H-Ras, GDP, farnesyl-Cys, and POPS are colored yellow, red (upper), blue, and red (lower).

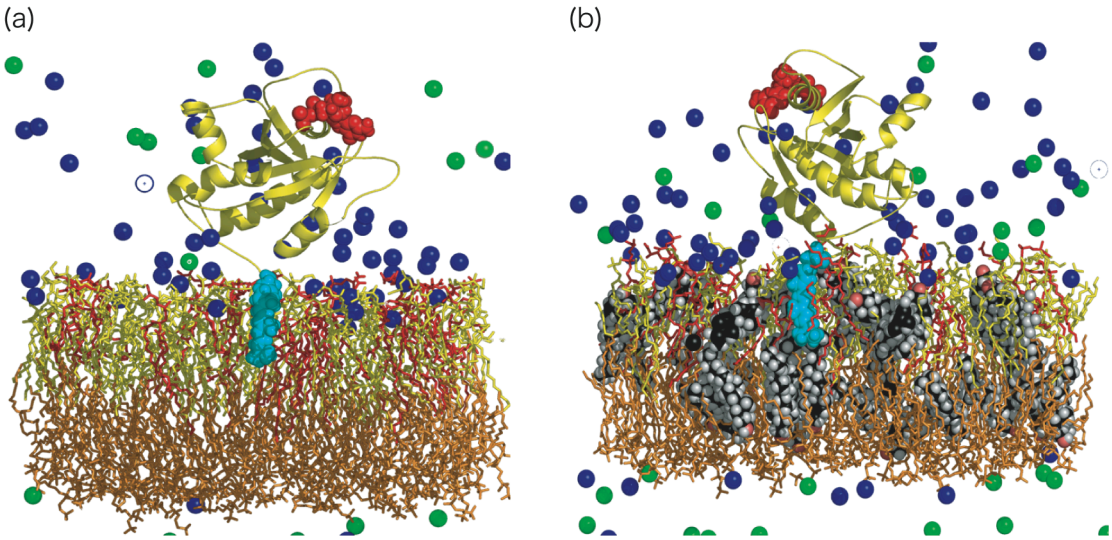

Figure 7.6 Structures of Far-Ras inserted in asymmetric bilayers.

(a) Asymmetric bilayer composed of POPC, POPE, and POPS. (b) Asymmetric bilayer composed of POPC, POPE, POPS, and cholesterol. Color schemes for lipids and ions are the same as Figure 4.3, and color schemes for proteins are the same as Figure 7.4.

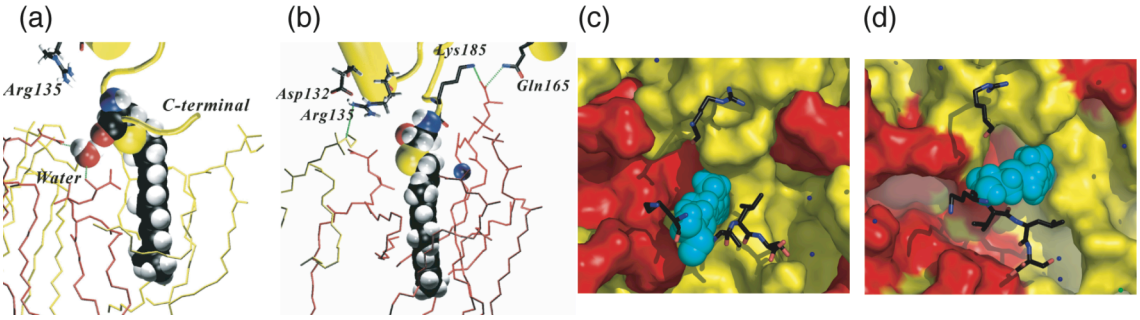

Figure 7.7 Detailed views of interactions between inserted Far-Ras and lipids.

(a) (b) Side views of the vicinities of the farnesyl-Cys residues. (c) (d) Top views of the membrane surfaces around the lipid anchors. Some C-terminal amino acid residues are also shown as sticks. ((a) POPC/POPE/POPS model; (b) POPC/POPE/POPS/cholesterol).

Far-Ras inserted in the membrane

Figure 7.6 shows the structures of Far-Ras inserted in the membranes after the MD simulations. More detailed views are shown in Figure 7.7. A part of the farnesyl moieties protrudes from the membranes. This protrusion is much clearer when viewed form the top (Figure 7.7 (c) and (d)). As a result, the farnesyl termini did not reach the center plane of the membranes. These results support the experimental results that a farnesyl moiety has relatively low affinity for membranes.[171,173] Figure 7.7 also shows that other amino acid residues interact with lipids.

VII.4 Conclusion

We have identified some important interactions between farnesylated H-Ras and lipids at the water-membrane interface. We have also shown that some of the Arg residues of H-Ras play an important role on the interaction. Although further studies are required in order to reveal the equilibrium mechanism of H-Ras moving between rafts and non-raft regions, these interactions between H-Ras and lipids will be necessary for the equilibrium.

Acknowledgment

本研究の遂行にあたり、終始御指導御鞭撻を賜りました、千葉大学大学院薬学研究院薬品物理化学研究室の根矢三郎教授、星野忠次助教授、畑晶之助手に謹んで御礼申し上げます。

また、数多くの御助言、御協力をいただきました、京都大学大学院薬学研究科薬品機能解析学分野の松崎勝巳教授に心から御礼申し上げます。

電子顕微鏡像を撮影するにあたり、御指導を賜りました千葉大学真菌医学研究センター機能形態分野の山口正視助教授に厚く御礼申し上げます。

本研究は、日本学術振興会特別研究員制度、ならびに、笹川科学研究助成の援助を受けて遂行されました。また、本研究は、薬品物理化学研究室の計算設備の他に、千葉大学総合メディア基盤センター、自然科学研究機構岡崎共通研究施設の計算科学研究センターの計算機を使用して行われました。これらの支援に、深く御礼申し上げます。

本論文の審査をしていただき、かつ多くの御助言を賜りました、千葉大学大学院薬学研究院生体分析化学研究室の戸井田敏彦教授、同研究院生化学研究室の小林弘教授、同研究院生物薬剤学研究室の堀江利治教授に御礼申し上げます。

長きに渡りお世話になりました、千葉大学大学院薬学研究院薬品物理化学研究室の卒業生、在学生の皆様に感謝いたします。

また、最後になりましたが、常に私を支えてくれた両親に、心より感謝の意を表します。

References

1. Lodish, H. et al. *Molecular Cell Biology*, 4th ed. (W. H. Freeman and Company, 2003).

2. Kraulis, P. MOLSCRIPT: a program to produce both detailed and schematic plots of protein structures. *J. Appl. Crystallogr.* **24**, 946-950 (1991).

3. Merritt, E.A. & Bacon, D.J. Raster3D: Photorealistic molecular graphics. *Meth. Enzymol.* **277**, 505-524 (1997).

4. Christie, W.W. The Lipid Library. http://www.lipidlibrary.co.uk/index.html

5. Matsumoto, K., Kusaka, J., Nishibori, A. & Hara, H. Lipid domains in bacterial membranes. *Mol. Microbiol.* **61**, 1110-1117 (2006).

6. Dowhan, W. MOLECULAR BASIS FOR MEMBRANE PHOSPHOLIPID DIVERSITY: Why Are There So Many Lipids? *Annu. Rev. Biochem.* **66**, 199 (1997).

7. Vance, J.E. & Steenbergen, R. Metabolism and functions of phosphatidylserine. *Prog. Lipid Res.* **44**, 207-234 (2005).

8. Chauhan, A., Ray, I. & Chauhan, V. Interaction of amyloid b-protein with anionic phospholipids: possible involvement of Lys28 and C-terminus aliphatic amino acids. *Neurochem. Res.* **25**, 423-9 (2000).

9. Stace, C.L. & Ktistakis, N.T. Phosphatidic acid- and phosphatidylserine-binding proteins. *Biochim. Biophys. Acta* **1761**, 913-26 (2006).

10. Cronan, J.E. BACTERIAL MEMBRANE LIPIDS: Where Do We Stand? *Annu. Rev. Microbiol.* **57**, 203-224 (2003).

11. Postle, A.D., Heeley, E.L. & Wilton, D.C. A comparison of the molecular species compositions of mammalian lung surfactant phospholipids. *Comp. Biochem. Physiol., Part A Mol. Integr. Physiol.* **129**, 65-73 (2001).

12. Gardocki, M.E., Jani, N. & Lopes, J.M. Phosphatidylinositol biosynthesis: biochemistry and regulation. *Biochim. Biophys. Acta* **1735**, 89-100 (2005).

13. Taylor, M.E. & Drickamer, K. *Introduction to Glycobiology*, 1st ed. (Oxford University Press, 2003).

14. Wang, X., Devaiah, S.P., Zhang, W. & Welti, R. Signaling functions of phosphatidic acid. *Prog. Lipid Res.* **45**, 250-78 (2006).

15. Nagan, N. & Zoeller, R. Plasmalogens: biosynthesis and functions. *Prog. Lipid. Res.* **40**, 199-229 (2001).

16. Brites, P., Waterham, H.R. & Wanders, R.J. Functions and biosynthesis of plasmalogens in health and disease. *Biochim. Biophys. Acta*. **1636**, 219-31 (2004).

17. Brugger, B. et al. The HIV lipidome: A raft with an unusual composition. *Proc. Natl. Acad. Sci. U.S.A.* **103**, 2641-2646 (2006).

18. Karlsson, K.A. Sphingolipid long chain bases. *Lipids* **5**, 878-891 (1970).

19. Hannun, Y.A. & Obeid, L.M. The Ceramide-centric universe of lipid-mediated cell regulation: stress encounters of the lipid kind. *J. Biol. Chem.* **277**, 25847-50 (2002).

20. Wertz, P.W. & van den Bergh, B. The physical, chemical and functional properties of lipids in the skin and other biological barriers. *Chem. Phys. Lipids* **91**, 85-96 (1998).

21. Chiu, S., Vasudevan, S., Jakobsson, E., Mashl, R.J. & Scott, H.L. Structure of sphingomyelin bilayers: a simulation study. *Biophys. J.* **85**, 3624-35 (2003).

22. Mombelli, E., Morris, R., Taylor, W. & Fraternali, F. Hydrogen-bonding propensities of sphingomyelin in solution and in a bilayer assembly: a molecular dynamics study. *Biophys. J.* **84**, 1507-17 (2003).

23. Simons, K. & Ikonen, E. Functional rafts in cell membranes. *Nature* **387**, 569-72 (1997).

24. Pitman, M., Suits, F., Mackerell, F. & Feller S.E. Molecular-level organization of saturated and polyunsaturated fatty acids in a phosphatidylcholine bilayer containing cholesterol. *Biochemistry* **43**, 15318-28 (2004).

25. Xu, F. et al. Dual roles for cholesterol in mammalian cells. *Proc. Natl. Acad. Sci. U.S.A.* **102**, 14551-6 (2005).

26. Maxfield, F.R. & Tabas, I. Role of cholesterol and lipid organization in disease. *Nature* **438**, 612-21 (2005).

27. Simons, K. & Toomre, D. Lipid rafts and signal transduction. *Nat. Rev. Mol. Cell. Biol.* **1**, 31-9 (2000).

28. Verkleij, A.J. & Post, J.A. Membrane Phospholipid Asymmetry and Signal Transduction. *J. Membr. Biol.* **178**, 1-10 (2000).

29. Paulusma, C.C. & Oude Elferink, R.P. Diseases of intramembranous lipid transport. *FEBS Lett.* **580**, 5500-9 (2006).

30. Holthuis, J.C. & Levine, T.P. Lipid traffic: floppy drives and a superhighway. *Nat. Rev. Mol. Cell. Biol.* **6**, 209-20 (2005).

31. Lee, A.G. Lipid-protein interactions in biological membranes: a structural perspective. *Biochim. Biophys. Acta* **1612**, 1-40 (2003).

32. Yuyama, K., Sekino-Suzuki, N., Sanai, Y. & Kasahara, K. Lipid rafts in cellular signaling and disease. *Trends Glycosci. Glycotechnol.* **15**, 139-151 (2003).

33. Rocks, O. et al. An acylation cycle regulates localization and activity of palmitoylated Ras isoforms. *Science* **307**, 1746-52 (2005).

34. Case, D.A. et al. AMBER 8. (2004).

35. Brooks, B.R. et al. CHARMM: A program for macromolecular energy, minimization, and dynamics calculations. *J. Comput. Chem.* **4**, 187-217 (1983).

36. Wang, J., Cieplak, P. & Kollman, P.A. How well does a restrained electrostatic potential (RESP) model perform in calculating conformational energies of organic and biological molecules? *J. Comput. Chem.* **21**, 1049-1074 (2000).

37. Duan, Y. et al. A point-charge force field for molecular mechanics simulations of proteins based on condensed-phase quantum mechanical calculations. *J. Comput. Chem.* **24**, 1999-2012 (2003).

38. Pandit, S. et al. Sphingomyelin-cholesterol domains in phospholipid membranes: atomistic simulation. *Biophys. J.* **87**, 1092-100 (2004).

39. Pandit, S.A., Jakobsson, E. & Scott, H.L. Simulation of the early stages of nano-domain formation in mixed bilayers of sphingomyelin, cholesterol, and dioleylphosphatidylcholine. *Biophys. J.* **87**, 3312-22 (2004).

40. Mori, K., Hata, M., Neya, S. & Hoshino, T. MD simulation of asymmetric phospholipid bilayers with ions and cholesterols. *CBI J* **4**, 15-26 (2004).

41. Pitman, M.C., Suits, F., MacKerell, A.D. & Feller, S.E. Molecular-level organization of saturated and polyunsaturated fatty acids in a phosphatidylcholine bilayer containing cholesterol. *Biochemistry* **43**, 15318-28 (2004).

42. Pasenkiewicz-Gierula, M., Rog, T., Kitamura, K. & Kusumi, A. Cholesterol Effects on the Phosphatidylcholine Bilayer Polar Region: A Molecular Simulation Study. *Biophys. J.* **78**, 1376-1389 (2000).

43. Feller, S.E. & MacKerell, J., A.D. An Improved Empirical Potential Energy Function for Molecular Simulations of Phospholipids. *J. Phys. Chem. B* **104**, 7510-7515 (2000).

44. Shinoda, W. & Okazaki, S. A Voronoi analysis of lipid area fluctuation in a bilayer. *J. Chem. Phys.* **109**, 1517-1521 (1998).

45. Feller, S.E., Yin, D., Pastor, R.W. & MacKerell, A.D. Molecular dynamics simulation of unsaturated lipid bilayers at low hydration: parameterization and comparison with diffraction studies. *Biophys. J.* **73**, 2269-79 (1997).

46. Takai, Y., Sasaki, T. & Matozaki, T. Small GTP-Binding Proteins. *Physiol. Rev.* **81**, 153-208 (2001).

47. Mori, K., Hata, M., Neya, S. & Hoshino, T. Common semiopen conformations of Mg^{2+}-free Ras, Rho, Rab, Arf, and Ran proteins combined with GDP and their similarity with GEF-bound forms. *J. Am. Chem. Soc.* **127**, 15127-37 (2005).

48. Humphrey, W., Dalke, A. & Schulten, K. VMD: visual molecular dynamics. *J. Mol. Graph.* **14**, 33-38 (1996).

49. Phillips, J.C. et al. Scalable molecular dynamics with NAMD. *J. Comput. Chem.* **26**, 1781-802 (2005).

50. Hashimoto, K. et al. KEGG as a glycome informatics resource. *Glycobiology* **16**, 63R-70R (2006).

51. Ellson, J. et al. Graphviz - Graph Visualization Software.

52. Loss, A. et al. SWEET-DB: an attempt to create annotated data collections for carbohydrates. *Nucleic. Acids Res.* **30**, 405-8 (2002).

53. Morris, G.M. et al. Automated docking using a Lamarckian genetic algorithm and an empirical binding free energy function. *J. Comput. Chem.* **19**, 1639-1662 (1998).

54. Makino, S. & Kuntz, I.D. Automated flexible ligand docking method and its application for database search. *J. Comput. Chem.* **18**, 1812-1825 (1997).

55. Verdonk, M.L., Cole, J.C., Hartshorn, M.J., Murray, C.W. & Taylor, R.D. Improved protein-ligand docking using GOLD. *Proteins* **52**, 609-23 (2003).

56. Yano, Y. & Matsuzaki, K. Measurement of thermodynamic parameters for hydrophobic mismatch 1: self-association of a transmembrane helix. *Biochemistry* **45**, 3370-8 (2006).

57. Yano, Y., Ogura, M. & Matsuzaki, K. Measurement of thermodynamic parameters for hydrophobic mismatch 2: intermembrane transfer of a transmembrane helix. *Biochemistry* **45**, 3379-85 (2006).

58. Killian, J.A. Hydrophobic mismatch between proteins and lipids in membranes. *Biochim. Biophys. Acta* **1376**, 401-15 (1998).

59. Gumbart, J. & Schulten, K. Molecular Dynamics Studies of the Archaeal Translocon. *Biophys. J.* **90**, 2356-2367 (2006).

60. Mathe, J., Aksimentiev, A., Nelson, D.R., Schulten, K. & Meller, A. Orientation discrimination of single-stranded DNA inside the a-hemolysin membrane channel. *Proc. Natl. Acad. Sci. U.S.A.* **102**, 12377-12382 (2005).

61. Aksimentiev, A. & Schulten, K. Imaging a-Hemolysin with Molecular Dynamics: Ionic Conductance, Osmotic Permeability, and the Electrostatic Potential Map. *Biophys. J.* **88**, 3745-3761 (2005).

62. Wang, Y., Schulten, K. & Tajkhorshid, E. What Makes an Aquaporin a Glycerol Channel? A Comparative Study of AqpZ and GlpF. *Structure* **13**, 1107-1118 (2005).

63. Gullingsrud, J. & Schulten, K. Lipid Bilayer Pressure Profiles and Mechanosensitive Channel Gating. *Biophys. J.* **86**, 3496-3509 (2004).

64. Cohen, J. & Schulten, K. Mechanism of Anionic Conduction across ClC. *Biophys. J.* **86**, 836-845 (2004).

65. Saam, J., Tajkhorshid, E., Hayashi, S. & Schulten, K. Molecular Dynamics Investigation of Primary Photoinduced Events in the Activation of Rhodopsin. *Biophys. J.* **83**, 3097-3112 (2002).

66. Spassov, V.Z., Yan, L. & Szalma, S. Introducing an Implicit Membrane in Generalized Born/Solvent Accessibility Continuum Solvent Models. *J. Phys. Chem. B* **106**, 8726-8738 (2002).

67. Im, W., Lee, M.S. & Brooks III, C.L. Generalized born model with a simple smoothing function. *J. Compt. Chem.* **24**, 1691-1702 (2003).

68. Tanizaki, S. & Feig, M. Molecular Dynamics Simulations of Large Integral Membrane Proteins with an Implicit Membrane Model. *J. Phys. Chem. B* **110**, 548-556 (2006).

69. Phillips, J. et al. Scalable molecular dynamics with NAMD. *J Comput Chem* **26**, 1781-802 (2005).

70. R Development Core Team. R: A language and environment for statistical computing. (2005). http://www.r-project.org/

71. Scott, D.W. & Sheather, S.J. Kernel density estimation with binned data. *Commun. Statist. -- Theory Meth.* **14**, 1353 (1985).

72. Zasloff, M. Antimicrobial peptides of multicellular organisms. *Nature* **415**, 389-395 (2002).

73. Matsuzaki, K. Mechanisms of innate immunity based on antimicrobial peptides. *Tanpakushitsu Kakusan Koso* **46**, 2060 (2001).

74. Matsuzaki, K. & Horikiri, C. Interactions of amyloid beta-peptide (1-40) with ganglioside-containing membranes. *Biochemistry* **38**, 4137-42 (1999).

75. Choo-Smith, L.P., Garzon-Rodriguez, W., Glabe, C.G. & Surewicz, W.K. Acceleration of amyloid fibril formation by specific binding of Ab-(1-40) peptide to ganglioside-containing membrane vesicles. *J. Biol. Chem.* **272**, 22987-90 (1997).

76. Tu, K., Klein, M.L. & Tobias, D.J. Constant-Pressure Molecular Dynamics Investigation of Cholesterol Effects in a Dipalmitoylphosphatidylcholine Bilayer. *Biophys. J.* **75**, 2147-2156 (1998).

77. Rog, T. & Pasenkiewicz-Gierula, M. Cholesterol Effects on the Phosphatidylcholine Bilayer Nonpolar Region: A Molecular Simulation Study. *Biophys. J.* **81**, 2190-2202 (2001).

78. Jorgensen, W.L., Chandrasekhar, J., Madura, J.D., Impey, R.W. & Klein, M.L. Comparison of simple potential functions for simulating liquid water. *J. Chem. Phys.* **79**, 926-935 (1983).

79. Grubmüller, H. SOLVATE 1.0. (1996). http://www.mpibpc.mpg.de/groups/grubmueller/start/software/solvate/docu.html

80. Feller, S.E., Gawrisch, K. & MacKerell, A.D. Polyunsaturated Fatty Acids in Lipid Bilayers: Intrinsic and Environmental Contributions to Their Unique Physical Properties. *J. Am. Chem. Soc.* **124**, 318-326 (2002).

81. Nose, S. A unified formulation of the constant temperature molecular dynamics methods. *J. Chem. Phys.* **81**, 511-519 (1984).

82. Hoover, W.G. Canonical dynamics: Equilibrium phase-space distributions. *Phys. Rev.* **31**, 1695-1697 (1985).

83. Yanagisawa, K., Odaka, A., Suzuki, N. & Ihara, Y. GM1 ganglioside-bound amyloid beta-protein (A beta): a possible form of preamyloid in Alzheimer's disease. *Nat Med* **1**, 1062-6 (1995).

84. Suzuki, Y. Gangliosides as influenza virus receptors. Variation of influenza viruses and their recognition of the receptor sialo-sugar chains. *Prog Lipid Res* **33**, 429-57 (1994).

85. Merritt, E. et al. The 1.25 A resolution refinement of the cholera toxin B-pentamer: evidence of peptide backbone strain at the receptor-binding site. *J Mol Biol* **282**, 1043-59 (1998).

86. McLaurin, J., Franklin, T., Fraser, P. & Chakrabartty, A. Structural transitions associated with the interaction of Alzheimer β-amyloid peptides with gangliosides. *J. Biol. Chem.* **273**, 4506-15 (1998).

87. Ariga, T. et al. Characterization of high-affinity binding between gangliosides and amyloid β -protein. *Arch. Biochem. Biophys.* **388**, 225-30 (2001).

88. Hayashi, H. et al. A seed for Alzheimer amyloid in the brain. *J. Neurosci.* **24**, 4894-902 (2004).

89. Kakio, A., Nishimoto, S., Yanagisawa, K., Kozutsumi, Y. & Matsuzaki, K. Cholesterol-dependent formation of GM1 ganglioside-bound amyloid β -protein, an endogenous seed for Alzheimer amyloid. *J. Biol. Chem.* **276**, 24985-90 (2001).

90. Shobab, L., Hsiung, G. & Feldman, H. Cholesterol in Alzheimer's disease. *Lancet Neurol.* **4**, 841-52 (2005).

91. Yamamoto, N., Hasegawa, K., Matsuzaki, K., Naiki, H. & Yanagisawa, K. Environment- and mutation-dependent aggregation behavior of Alzheimer amyloid β -protein. *J. Neurochem.* **90**, 62-9 (2004).

92. Kakio, A. et al. Interaction between amyloid β -protein aggregates and membranes. *J. Pept. Sci.* **10**, 612-21 (2004).

93. Yamamoto, N., Matsuzaki, K. & Yanagisawa, K. Cross-seeding of wild-type and hereditary variant-type amyloid β -proteins in the presence of gangliosides. *J. Neurochem.* **95**, 1167-76 (2005).

94. Momany, F.A. & Rone, R. Validation of the general purpose QUANTA/CHARMm force field. *J. Comput. Chem.* **13**, 888-900 (1992).

95. Nicholls, A., Sharp, K. & Honig, B. Protein folding and association: insights from the interfacial and thermodynamic properties of hydrocarbons. *Proteins* **11**, 281-96 (1991).

96. Ferraretto, A., Pitto, M., Palestini, P. & Masserini, M. Lipid domains in the membrane: thermotropic properties of sphingomyelin vesicles containing GM1 ganglioside and cholesterol. *Biochemistry* **36**, 9232-6 (1997).

97. Mehlhorn, I., Florio, E., Barber, K., Lordo, C. & Grant, C. Evidence that trans-bilayer interdigitation of glycosphingolipid long chain fatty acids may be a general phenomenon. *Biochim. Biophys. Acta* **939**, 151-9 (1988).

98. Scarsdale, J., Prestegard, J. & Yu, R. NMR and computational studies of interactions between remote residues in gangliosides. *Biochemistry* **29**, 9843-55 (1990).

99. Wang, S., Rymer, D. & Good, T. Reduction in cholesterol and sialic acid content protects cells from the toxic effects of β -amyloid peptides. *J. Biol. Chem.* **276**, 42027-34 (2001).

100. Ryhanen, S., Alakoskela, J. & Kinnunen, P. Increasing surface charge density induces interdigitation in vesicles of cationic amphiphile and phosphatidylcholine. *Langmuir* **21**, 5707-15 (2005).

101. Thompson, T., Allietta, M., Brown, R., Johnson, M. & Tillack, T. Organization of ganglioside GM1 in phosphatidylcholine bilayers. *Biochim. Biophys. Acta* **817**, 229-37 (1985).

102. Filippov, A. & Or. The effect of cholesterol on the lateral diffusion of phospholipids in oriented bilayers. *Biophys. J.* **84**, 3079-86 (2003).

103. Goins, B., Masserini, M., Barisas, B. & Freire, E. Lateral diffusion of ganglioside GM1 in phospholipid bilayer membranes. *Biophys. J.* **49**, 849-56 (1986).

104. Tocanne, J., Dupou-Cezanne, L. & Lopez, A. Lateral diffusion of lipids in model and natural membranes. *Prog. Lipid. Res.* **33**, 203-37 (1994).

105. Wu, E., Jacobson, K. & Papahadjopoulos, D. Lateral diffusion in phospholipid multibilayers measured by fluorescence recovery after photobleaching. *Biochemistry* **16**, 3836-41 (1977).

106. Schram, V. & Thompson, T. Interdigitation does not affect translational diffusion of lipids in liquid crystalline bilayers. *Biophys. J.* **69**, 2517-20 (1995).

107. Lindblom, G., Johansson, L. & Arvidson, G. Effect of cholesterol in membranes. Pulsed nuclear magnetic resonance measurements of lipid lateral diffusion. *Biochemistry* **20**, 2204-7 (1981).

108. Gaede, H. & Gawrisch, K. Lateral diffusion rates of lipid, water, and a hydrophobic drug in a multilamellar liposome. *Biophys. J.* **85**, 1734-40 (2003).

109. Sujatha, M. & Balaji, P. Identification of common structural features of binding sites in galactose-specific proteins. *Proteins* **55**, 44-65 (2004).

110. Sujatha, M., Sasidhar, Y. & Balaji, P. Insights into the role of the aromatic residue in galactose-binding sites: MP2/6-311G++** study on galactose- and glucose-aromatic residue analogue complexes. *Biochemistry* **44**, 8554-62 (2005).

111. Chen, C., Song, S., Gilboa-Garber, N., Chang, K. & Wu, A. Studies on the binding site of the galactose-specific agglutinin PA-IL from *Pseudomonas aeruginosa*. *Glycobiology* **8**, 7-16 (1998).

112. Chachaty, C., Rainteau, D., Tessier, C., Quinn, P. & Wolf, C. Building up of the liquid-ordered phase formed by sphingomyelin and cholesterol. *Biophys J* **88**, 4032-44 (2005).

113. Tierney, K., Block, D. & Longo, M. Elasticity and phase behavior of DPPC membrane modulated by cholesterol, ergosterol, and ethanol. *Biophys. J.* **89**, 2481-93 (2005).

114. Kakio, A., Nishimoto, S., Yanagisawa, K., Kozutsumi, Y. & Matsuzaki, K. Interactions of amyloid β -protein with various gangliosides in raft-like membranes: importance of GM1 ganglioside-bound form as an endogenous seed for Alzheimer amyloid. *Biochemistry* **41**, 7385-90 (2002).

115. Ben-Tal, N., Honig, B., Peitzsch, R., Denisov, G. & McLaughlin, S. Binding of small basic peptides to membranes containing acidic lipids: theoretical models and experimental results. *Biophys. J.* **71**, 561-75 (1996).

116. Ben-Tal, N., Honig, B., Miller, C. & McLaughlin, S. Electrostatic binding of proteins to membranes. Theoretical predictions and experimental results with charybdotoxin and phospholipid vesicles. *Biophys. J.* **73**, 1717-27 (1997).

117. Langner, M. & Kubica, K. The electrostatics of lipid surfaces. *Chem. Phys. Lipids* **101**, 3-35 (1999).

118. Terzi, E., Holzemann, G. & Seelig, J. Self-association of β-amyloid peptide (1-40) in solution and binding to lipid membranes. *J. Mol. Biol.* **252**, 633-42 (1995).

119. Choo-Smith, L. & Surewicz, W. The interaction between Alzheimer amyloid β (1-40) peptide and ganglioside GM1-containing membranes. *FEBS Lett.* **402**, 95-8 (1997).

120. Talafous, J., Marcinowski, K., Klopman, G. & Zagorski, M. Solution structure of residues 1-28 of the amyloid β-peptide. *Biochemistry* **33**, 7788-96 (1994).

121. Crescenzi, O. et al. Solution structure of the Alzheimer amyloid β-peptide (1-42) in an apolar microenvironment. Similarity with a virus fusion domain. *Eur. J. Biochem.* **269**, 5642-8 (2002).

122. Katagiri, D., Tsuchiya, T., Tsuda, M., Hata, M. & Hoshino, T. Computational Analysis of Stability of the β-Sheet Structure. *J. Phys. Chem.. B* **106**, 9151-9158 (2002).

123. Cruz, L. et al. Solvent and mutation effects on the nucleation of amyloid β-protein folding. *Proc. Natl. Acad. Sci. U.S.A.* **102**, 18258-63 (2005).

124. Vetter, I.R. & Wittinghofer, A. The Guanine Nucleotide-Binding Switch in Three Dimensions. *Science* **294**, 1299-1304 (2001).

125. Bar-Sagi, D. & Feramisco, J.R. Microinjection of the ras oncogene protein into PC12 cells induces morphological differentiation. *Cell* **42**, 841-848 (1985).

126. Hagag, N., Halegoua, S. & Viola, M. Inhibition of growth factor-induced differentiation of PC12 cells by microinjection of antibody to ras p21. *Nature* **319**, 680-682 (1986).

127. Feramisco, J.R., Gross, M., Kamata, T., Rosenberg, M. & Sweet, R.W. Microinjection of the oncogene form of the human H-ras (t-24) protein results in rapid proliferation of quiescent cells. *Cell* **38**, 109-117 (1984).

128. Kauffmann-Zeh, A. et al. Suppression of c-Myc-induced apoptosis by Ras signalling through PI(3)K and PKB. *Nature* **385**, 544-548 (1997).

129. Etienne-Manneville, S. & Hall, A. Rho GTPases in cell biology. *Nature* **420**, 629-635 (2002).

130. Yuan, X. et al. Signalling and crosstalk of Rho GTPases in mediating axon guidance. *Nat. Cell Biol.* **5**, 38-45 (2003).

131. Novick, P. & Zerial, M. The diversity of Rab proteins in vesicle transport. *Curr. Opin. Cell Biol.* **9**, 496-504 (1997).

132. Dasso, M. The Ran GTPase: Theme and Variations. *Curr. Biol.* **12**, R502-R508 (2002).

133. Lenzen, C., Cool, R.H., Prinz, H., Kuhlmann, J. & Wittinghofer, A. Kinetic Analysis by Fluorescence of the Interaction between Ras and the Catalytic Domain of the Guanine Nucleotide Exchange Factor Cdc25Mm *Biochemistry* **37**, 7420-7430 (1998).

134. Klebe, C., Prinz, H., Wittinghofer, A. & Goody, R.S. The Kinetic Mechanism of Ran-Nucleotide Exchange Catalyzed by RCC1. *Biochemistry* **34**, 12543-12552 (1995).

135. Boriack-Sjodin, P.A., Margarit, S.M., Bar-Sagi, D. & Kuriyan, J. The structural basis of the activation of Ras by Sos. *Nature* **394**, 337-343 (1998).

136. Goldberg, J. Structural Basis for Activation of ARF GTPase: Mechanisms of Guanine Nucleotide Exchange and GTP-Myristoyl Switching. *Cell* **95**, 237-248 (1998).

137. Renault, L., Kuhlmann, J., Henkel, A. & Wittinghofer, A. Structural Basis for Guanine Nucleotide Exchange on Ran by the Regulator of Chromosome Condensation (RCC1). *Cell* **105**, 245-255 (2001).

138. Snyder, J.T. et al. Structural basis for the selective activation of Rho GTPases by Dbl exchange factors. *Nat. Struct. Mol. Biol.* **9**, 468-475 (2002).

139. John, J. et al. Kinetic and structural analysis of the Mg^{2+}-binding site of the guanine nucleotide-binding protein p21H-ras. *J. Biol. Chem.* **268**, 923-929 (1993).

140. Hall, A. & Self, A.J. The effect of Mg^{2+} on the guanine nucleotide exchange rate of p21N-ras. *J. Biol. Chem.* **261**, 10963-10965 (1986).

141. Panniers, R., Rowlands, A.G. & Henshaw, E.C. The effect of Mg^{2+} and guanine nucleotide exchange factor on the binding of guanine nucleotides to eukaryotic initiation factor 2. *J. Biol. Chem.* **263**, 5519-5525 (1988).

142. Pan, J.Y., Sanford, J.C. & Wessling-Resnick, M. Influence of Mg^{2+} on the Structure and Function of Rab5. *J. Biol. Chem.* **271**, 1322-1328 (1996).

143. Burstein, E.S. & Macara, I.G. Interactions of the ras-like protein p25rab3A with Mg^{2+} and guanine nucleotides. *Biochem. J.* **282**, 387 (1992).

144. Shimizu, T. et al. An Open Conformation of Switch I Revealed by the Crystal Structure of a Mg^{2+}-free Form of RHOA Complexed with GDP. IMPLICATIONS FOR THE GDP/GTP EXCHANGE MECHANISM. *J. Biol. Chem.* **275**, 18311-18317 (2000).

145. Shutes, A., Phillips, R.A., Corrie, J.E.T. & Webb, M.R. Role of Magnesium in Nucleotide Exchange on the Small G Protein Rac Investigated Using Novel Fluorescent Guanine Nucleotide Analogues. *Biochemistry* **41**, 3828-3835 (2002).

146. Milburn, M.V. et al. Molecular switch for signal transduction: structural differences between active and inactive forms of protooncogenic ras proteins. *Science* **247**, 939-945 (1990).

147. Wei, Y. et al. Crystal structure of RhoA-GDP and its functional implications. *Nat. Struct. Mol. Biol.* **4**, 699-703 (1997).

148. Chattopadhyay, D. et al. Structure of the nucleotide-binding domain of Plasmodium falciparum Rab6 in the GDP-bound form. *Acta Crystallogr. D Biol. Crystallogr.* **56**, 937-944 (2000).

149. Amor, J.C., Harrison, D.H., Kahn, R.A. & Ringe, D. Structure of the human ADP-ribosylation factor 1 complexed with GDP. *Nature* **372**, 704-708 (1994).

150. Stewart, M., Kent, H.M. & McCoy, A.J. The structure of the Q69L mutant of GDP-ran shows a major conformational change in the switch II loop that accounts for its failure to bind nuclear transport factor 2 (NTF2). *J. Mol. Biol.* **284**, 1517-1527 (1998).

151. Alexov, E.G. & Gunner, M.R. Calculated Protein and Proton Motions Coupled to Electron Transfer: Electron Transfer from QA- to QB in Bacterial Photosynthetic Reaction Centers. *Biochemistry* **38**, 8253-8270 (1999).

152. Berendsen, H.J.C., Postma, J.P.M., van Gunsteren, W.F., DiNola, A. & Haak, J.R. Molecular dynamics with coupling to an external bath. *J. Chem. Phys.* **81**, 3684-3690 (1984).

153. Ryckaert, J.P., Ciccotti, G. & Berendsen, H.J.C. Numerical integration of the cartesian equations of motion of a system with constraints: molecular dynamics of n-alkanes. *J. Comput. Phys.* **23**, 327-341 (1977).

154. Koradi, R., Billeter, M. & Wuthrich, K. MOLMOL: A program for display and analysis of macromolecular structures. *J. Mol. Graph.* **14**, 51-55 (1996).

155. Nakano, T. et al. Fragment molecular orbital method: application to polypeptides. *Chem. Phys. Lett.* **318**, 614-618 (2000).

156. Farnsworth, C.L. & Feig, L.A. Dominant inhibitory mutations in the Mg^{2+}-binding site of RasH prevent its activation by GTP. *Mol. Cell. Biol.* **11**, 4822-4829 (1991).

157. de Vendittis, E., Zahn, R. & Fasano, O. Regeneration of the GTP-bound from the GDP-bound form of human and yeast ras proteins by nucleotide exchange. Stimulatory effect of organic and inorganic polyphosphates. *Eur. J. Biochem.* **161**, 473-478 (1986).

158. Burstein, E.S., Brondyk, W.H. & Macara, I.G. Amino acid residues in the Ras-like GTPase Rab3A that specify sensitivity to factors that regulate the GTP/GDP cycling of Rab3A. *J. Biol. Chem.* **267**, 22715-22718 (1992).

159. Kornbluth, S., Dasso, M. & Newport, J. Evidence for a dual role for TC4 protein in regulating nuclear structure and cell cycle progression. *J. Cell Biol.* **125**, 705-719 (1994).

160. Zhang, B., Zhang, Y., Wang, Z. & Zheng, Y. The Role of Mg^{2+} Cofactor in the Guanine Nucleotide Exchange and GTP Hydrolysis Reactions of Rho Family GTP-binding Proteins. *J. Biol. Chem.* **275**, 25299-25307 (2000).

161. Pan, J.Y. & Wessling-Resnick, M. GEF-mediated GDP/GTP exchange by monomeric GTPases: A regulatory role for Mg^{2+}? *BioEssays* **20**, 516-521 (1998).

162. Landino, L.M. & Macdonald, T.L. Inhibition of the GDP/GTP exchange reaction of ras p21 by aluminium ion. *J. Inorg. Biochem.* **66**, 99-102 (1997).

163. Scheffzek, K., Stephan, I., Jensen, O.N., Illenberger, D. & Gierschik, P. The Rac-RhoGDI complex and the structural basis for the regulation of Rho proteins by RhoGDI. *Nat. Struct. Mol. Biol.* **7**, 122-126 (2000).

164. Hall, B.E., Yang, S., Boriack-Sjodin, P.A., Kuriyan, J. & Bar-Sagi, D. Structure-based Mutagenesis Reveals Distinct Functions for Ras Switch 1 and Switch 2 in Sos-catalyzed Guanine Nucleotide Exchange. *J. Biol. Chem.* **276**, 27629-27637 (2001).

165. Hancock, J.F. Ras proteins: different signals from different locations. *Nat. Rev. Mol. Cell. Biol.* **4**, 373-84 (2003).

166. Prior, I.A. et al. GTP-dependent segregation of H-ras from lipid rafts is required for biological activity. *Nat. Cell. Biol.* **3**, 368-75 (2001).

167. Prior, I.A., Muncke, C., Parton, R.G. & Hancock, J.F. Direct visualization of Ras proteins in spatially distinct cell surface microdomains. *J. Cell. Biol.* **160**, 165-70 (2003).

168. Niv, H., Gutman, O., Kloog, Y. & Henis, Y. Activated K-Ras and H-Ras display different interactions with saturable nonraft sites at the surface of live cells. *J. Cell. Biol.* **157**, 865-72 (2002).

169. Rotblat, B. et al. Three separable domains regulate GTP-dependent association of H-ras with the plasma membrane. *Mol. Cell. Biol.* **24**, 6799-810 (2004).

170. Roy, S. et al. Individual palmitoyl residues serve distinct roles in H-ras trafficking, microlocalization, and signaling. *Mol. Cell. Biol.* **25**, 6722-33 (2005).

171. Hancock, J.F. & Parton, R.G. Ras plasma membrane signalling platforms. *Biochem J* **389**, 1-11 (2005).

172. Wong, M.W., Frisch, M.J. & Wiberg, K.B. Solvent effects. 1. The mediation of electrostatic effects by solvents. *J. Am. Chem. Soc.* **113**, 4776-4782 (1991).

173. Meister, A. et al. Insertion of Lipidated Ras Proteins into Lipid Monolayers Studied by Infrared Reflection Absorption Spectroscopy (IRRAS). *Biophys. J.* **91**, 1388-1401 (2006).

Publications & Presentations

主論文目録

本学位論文の内容は下記の発表論文による。

Publications

1. <u>Kenichi Mori</u>, Masayuki Hata, Saburo Neya, Tyuji Hoshino

A Study on the Role of Mg^{2+} in a Ras Protein by MD Simulation

Chem-Bio Informatics Journal, **2**, 147-155 (2002)

2. <u>Kenichi Mori</u>, Masayuki Hata, Saburo Neya, Tyuji Hoshino

MD Simulation of Asymmetric Phospholipid Bilayers with Ions and Cholesterols

Chem-Bio Informatics Journal, **4**, 15-26 (2004)

3. <u>Kenichi Mori</u>, Masayuki Hata, Saburo Neya, Tyuji Hoshino

Common Semiopen Conformations of Mg^{2+}-free Ras, Rho, Rab, Arf, and Ran Proteins Combined with GDP and Their Similarity with GEF-bound Forms

Journal of American Chemical Society, **127**, 15127-15137 (2005)

Oral Presentations

1. **森　健一，畑　晶之，根矢三郎，星野忠次**

Mg^{2+}の配位による低分子量 G タンパク質の構造変化における分子動力学的研究

フィジカルファーマフォーラム 2003（PPF2003）要旨集，32（2003）

2. **森　健一，畑　晶之，根矢三郎，星野忠次**

生体内イオン・コレステロール濃度下における非対称性リン脂質二重膜に結合した Ras タンパク質の分子動力学シミュレーション

第 26 回日本分子生物学会年会プログラム，63（2003）

3. **森　健一，畑　晶之，根矢三郎，星野忠次**

非対称性リン脂質二重膜の構築プログラムの開発とシミュレーションへの応用

フィジカルファーマフォーラム 2004（PPF2004）要旨集，AIII-5（2004）

4. **森　健一，高岡　翼，岩本　光司，畑　晶之，根矢三郎，星野忠次**

脂質マイクロドメインを指向した糖鎖・膜モデル化プログラムの構築とシミュレーションへの応用

フィジカルファーマフォーラム 2005（PPF2005）要旨集，16-17（2005）

5. **森　健一，畑　晶之，根矢三郎，星野忠次**

糖鎖・生体膜モデルの分子動力学シミュレーション

日本機械学会第 18 回計算力学講演会講演論文集［05-2］，441-442（2005）

6. **森　健一，高岡　翼，岩本　光司，畑　晶之，根矢三郎，星野忠次**

糖鎖・生体膜自動モデル化プログラムの構築とシミュレーションへの応用

日本膜学会膜シンポジウム 2005 プログラム集 (2005)

7. **森　健一，星野忠次**

生体膜ー膜タンパク質複合体モデルの自動作成プログラムの開発

フィジカルファーマフォーラム 2006（PPF2006）講演要旨集,18-19（2006）

8. **森　健一，高岡　翼，岩本　光司，畑　晶之，根矢三郎，星野忠次**

分子動力学シミュレーションによるモデル膜の解析

日本膜学会膜シンポジウム 2006 プログラム集, 117 (2006)

9. **星野忠次，森　健一**

糖鎖生体膜シミュレーションモデルによる膜タンパク質の挙動解析

第 26 回表面科学講演大会講演要旨集，33（2006）

Poster Presentations

1. 森　健一，長張健太郎，畑　晶之，根矢三郎，星野忠次

Ras の Sos による GDP-GTP 交換反応機構

日本薬学会第 122 年会要旨集– 3，13（2002）

2. 森　健一，畑　晶之，根矢三郎，星野忠次

MDシミュレーションによる低分子量Gタンパク質におけるMg^{2+}の役割に関する研究

第三回情報計算化学生物学会大会論文集，124-125（2002）

3. 森　健一，畑　晶之，根矢三郎，星野忠次

Mg の解離による低分子量 G 蛋白質の構造変化と GDP/GTP 交換反応との相関

日本薬学会第 123 年会要旨集– 3，32（2003）

4. Kenichi Mori, Masayuki Hata, Saburo Neya, Tyuji Hoshino

A Study on the Role of Mg^{2+} Ion in Small G-Proteins by MD Simulations

International Symposium on Molecular Nano-Engineering and Its Development into Microsystems - Chemical Nanoprocesses for Molecular Nanoengineering -, Tokyo, Japan, Abstracts, PA-10 (2003)

5. 森　健一，畑　晶之，根矢三郎，星野忠次

Mg^{2+}による低分子量 G タンパク質の構造制御機構に関する分子動力学的研究

第 7 回理論化学討論会講演要旨集，2P25（2003）

6. 森　健一，畑　晶之，根矢三郎，星野忠次

低分子量 G タンパク質の Mg^{2+}による制御機構に関する分子動力学的研究

日本コンピュータ化学会 2003 春季年会講演予稿集，1P26（2003）

7. 森　健一，畑　晶之，根矢三郎，星野忠次

MD シミュレーションによる低分子量 G タンパク質における Mg の役割に関する研究

第 13 回金属の関与する生体関連反応シンポジウム講演要旨集，118（2003）

8. **森　健一，畑　晶之，根矢三郎，星野忠次**

細胞内イオン濃度・コレステロール濃度を反映した非対称性（POPC/POPE・POPS）リン脂質二重膜の MD シミュレーション

情報計算化学生物（CBI）学会 2003 年大会予稿集，137-138（2003）

9. **森　健一，畑　晶之，根矢三郎，星野忠次**

Mg^{2+}イオンと生体膜との相互作用の分子動力学シミュレーションによる解明

日本薬学会第 124 年会要旨集−３，30（2004）

10. **森　健一，畑　晶之，根矢三郎，星野忠次**

糖鎖自動構築プログラムの開発とシミュレーションへの応用

情報計算化学生物学会 2004 年大会予稿集，98-99 (2004)

11. **森　健一，星野忠次**

生体脂質二重膜および糖鎖のモデリングツール

ナノテクノロジーフォーラム・ジョイントフェアー2004 予稿集，32 (2004)

12. **森　健一，畑　晶之，根矢三郎，星野忠次**

GM1/コレステロール/リン脂質混合系の分子動力学シミュレーション

日本生物物理学会第 42 年会講演予稿集，S79（2004）

13. **森　健一，星野忠次**

アミロイドβタンパク質と細胞膜との相互作用シミュレーション

早稲田大学 COE「分子ナノ工学拠点形成」公開シンポジウム (2005)

14. **Kenichi Mori, Yusuke Imai, Tsubasa Takaoka, Koji Iwamoto, Hideyoshi Fuji, Saburo Neya, Tyuji Hoshino**

Database of Lipid Membrane Structures: Computational Analyses of Model Membranes

Fifth East Asian Biophysics Symposium & Forty-Fourth Annual Meeting of the Biophysical Society of Japan, Okinawa, Japan

Meeting Program, 2P270 (2006)

生体膜と膜タンパク質の分子動力学シミュレーション

ゲノム機能学講座　（薬品物理化学研究室）　森　健一

1. 序論

薬物の標的タンパク質の多くは、膜タンパク質である。近年、膜タンパク質の機能解析や薬物設計を目的として、膜タンパク質ー生体膜複合体の分子動力学（MD）シミュレーションが行われてきている。しかし、これらの多くは、生体膜の構成を単純な脂質で近似して計算しており、脂質–タンパク質間相互作用を軽視している。この問題は、多くの X 線結晶構造があるタンパク質と異なり、脂質二重膜の３次元構造が手に入りづらいことに起因している。生体膜は、様々な脂質や膜タンパク質の混合物である上に、脂質の側方分離、外側と内側で脂質の構成が異なる、など複雑な構造を持っており、３次元構造をコンピュータ内に作り出すことも困難を極める。

2. 糖鎖・生体膜の分子モデリング

自動構築プログラム GLYMM の開発

そこでまず、糖鎖・脂質膜の３次元構造を自動的に構築するプログラム GLYMM（GLYcan and Membrane Modeling）の開発に着手した (Fig. 1)。GLYMM は GUI を備えており、マウスの操作のみで複雑な生体膜モデルを自動構築できる。また、糖鎖の初期構造を糖鎖の配列情報のみから構築することができ、作成した糖鎖を脂質やタンパク質に結合させることもできる。さらに、膜タンパク質を膜に埋め込む操作も、タンパク質と膜の慣性主軸および重心を一致させることで、自動化することに成功した。

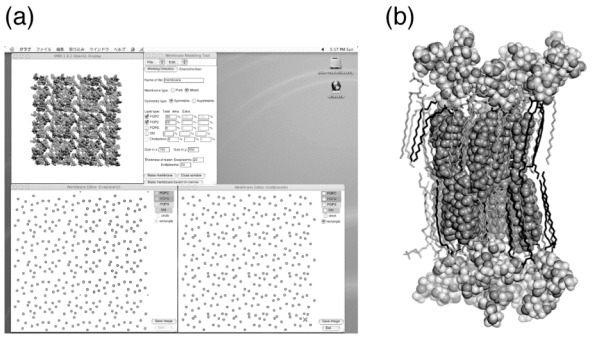

Fig.1 Membrane modeling by GLYMM
(a) Snapshot of GLYMM running on Mac OS X. (b) Glycosphingolipid membrane built by GLYMM.

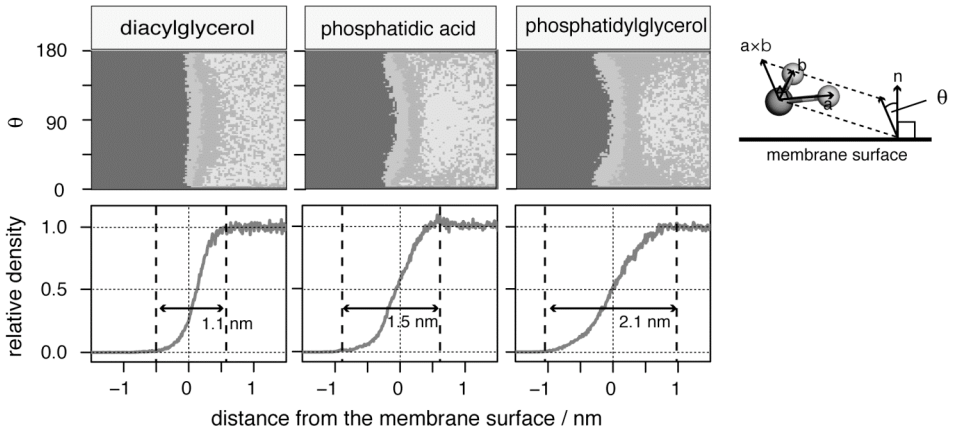

Fig.2 Orientation and distribution of water molecules at the water-membrane interface.
The upper row shows the distribution of the angle formed between the membrane normal vector (**n**) and the cross product (**a×b**) of two OH bonds (**a** and **b**). The lower row shows the distribution of the number of water molecules at the interface. The dashed lines indicate the range of the interface.

3. 生体膜の分子動力学シミュレーション

GLYMM のこれらの機能を用いて、様々な脂質膜を作成し、MD シミュレーションを行った。

3.1 対称的な脂質構成を持つ脂質二重膜

グリセロ脂質系列35種類、スフィンゴ脂質系列48種類のMDシミュレーションを行い、ゲル相、液晶相、interdigitatedゲル相などの様々な相状態を再現することができた。さらに、脂質の違いが膜の構造にどのような変化を与えるかを調べた。その結果、界面の水分子の分布や電荷密度は脂質頭部に依存し、アルキル鎖部分の影響や相状態の影響はほぼ無かった。また、水分子は膜界面で膜に平行になる傾向があり、脂質頭部が大きいほど、つまり、界面の幅が広いほど、その傾向は強かった (Fig. 2)。

3.2 非対称的な脂質構成を持つ脂質二重膜

より生体膜に近づけるため、脂質構成比が分かっている赤血球の細胞膜の構成比を基に非対称的な脂質膜のMDシミュレーションを行った(Fig.3)。計算したモデルは、細胞外側をPOPC、細胞内側をPOPE:POPS=2:1の比で構成した。さらに、コレステロール(Chol)の膜への影響を調べるため、Cholを追加したモデルも併せてシミュレーションを行った。その結果、膜界面にNa^+イオンが非対称的に分布し、POPS分子に沿うように分布していた。Cholが持つ、アルキル鎖の整然さを上昇させる効果も観察され、これは実験事実を反映していた。

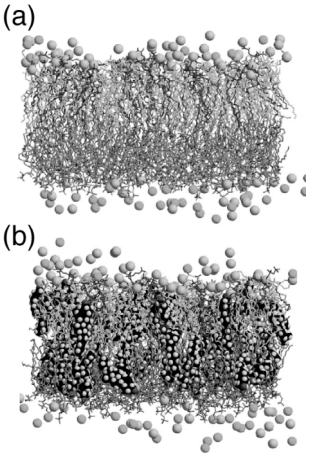

Fig.3 Asymmetric bilayers
(a) without cholesterol
(b) with cholesterol

3.3 糖脂質二重膜

ガングリオシド GM1、sphingomyelin (SM)、Chol が形成する脂質マイクロドメインの特徴を調べるため、GM1/SM/Chol = 1:2:2 の比で構成した model 1 と、GM1/POPC = 1:4 の比で構成した model 2 の２種類の MD シミュレーションを行った。この 2 つのモデル膜は、model 1 には Amyloid β (Aβ) ペプチドが結合するのに対し、model 2 には結合しないという実験事実がある。シミュレーションの結果、model 1 では GM1 の糖鎖部分がクラスターを形成したのに対し、model 2 では GM1 の糖鎖部分は膜面上に散逸したままであった (Fig. 4)。さらに、GM1 の糖鎖にあるシアル酸の carboxyl 基が、高い確率で一定の間隔に配列することが分かった。この間隔は、Aβペプチドがβ–sheet conformation をとったときの主鎖の NH の間隔と一致していた。また、他の酸性脂質膜の電荷密度とは異なる、負電荷の集中した特徴的な領域を膜界面に形成していた。これらの結果から、シアル酸の配列が GM1-Aβの形成を促進するというメカニズムを示唆することができた。

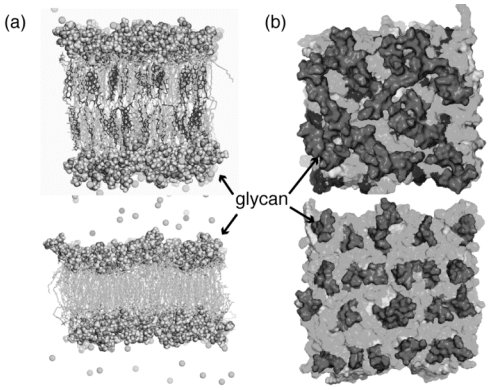

Fig. 4 Ganglioside GM1-containing bilayers.
(a) Side views (b) Top views. (upper, model 1; lower, model 2)

4. 膜タンパク質の分子動力学シミュレーション

次に、膜タンパク質である低分子量 G タンパク質(GNBP)のシミュレーションを行った。低分子量 G タンパク質としては、H-Ras, RhoA, Rab6, Arf1, Ran を用いた。Ran 以外の 4 種類が脂質アンカー型膜タンパク質である。

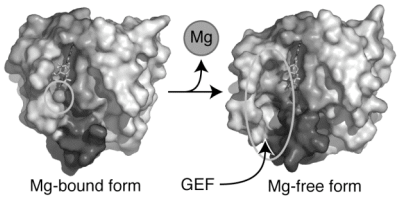

Fig.5 Conformational change of a small G-protein by removal of Mg^{2+} ion.

4.1 水溶液中での GNBP の MD シミュレーション

まず、水溶液中でのシミュレーションを行い、その構造変化が Mg^{2+}イオンや、アミノ酸のプロトン化状態によって、どれほど影響を受けるかを調べた。その結果、Mg^{2+}イオンの除去により GNBP は GDP-GTP 交換促進因子 GEF と結合しやすい構造へと構造変化した (Fig.5) が、この変化はタンパク質がアミノ酸のプロトン化状態を変えることで緩衝された。このシミュレーションにより、GNBP の周りの電場が、その構造変化に重要な働きをしていることが示唆された。

4.2 膜界面での H-Ras の MD シミュレーション

最後に、3.2 の細胞膜モデル界面に H-Ras タンパク質を配置し、MD シミュレーションを行い、タンパク質ー脂質膜間の相互作用、および、それぞれの構造変化を調べた。その結果、H-Ras は、GDP 結合部位を膜から遠くなるように配置し、脂質アンカーを膜方向に向けて安定化した。これは、膜界面の負の静電場と H-Ras の GDP 結合部位周辺の負電荷に反発力が働くが、脂質アンカー周辺のアルギニン(Arg)残基と酸性脂質の PS 間に強い引力が働くために生じたものと考察される。PS 分子が Arg 残基と相互作用するために膜面から飛び出すことも観察された。

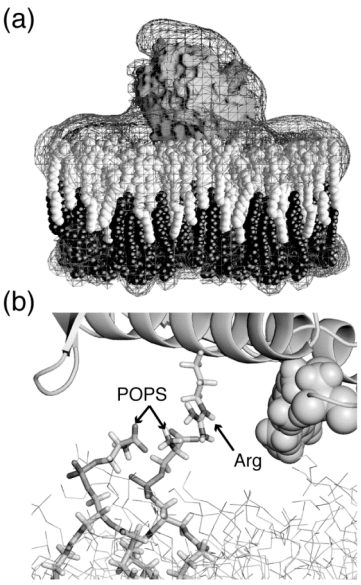

Fig. 6 H-Ras on a lipid bilayer (a) Electrostatic potential of Ras-membrane complex. (b) Arg-POPS interaction.

5. 総括

本研究で開発した糖鎖・生体膜モデル自動構築プログラム GLYMM は生体膜・膜タンパク質のシミュレーション研究を推進するものと考えられる。また、膜タンパク質は、生体膜の静電場、誘電率、界面での水分子の分布など、様々な影響を受け、構造変化を起こしている。本研究で、その一端を原子レベルで明らかにできたものと確信している。

6. 文献

(1) Mori, K., Hata, M., Neya S., Hoshino, T.: A Study on the Role of Mg^{2+} in a Ras Protein by MD Simulation, *Chem-Bio Informatics Journal*, 2, 147-155 (2002)

(2) Mori, K., Hata, M., Neya S., Hoshino, T.: MD Simulation of Asymmetric Phospholipid Bilayers with Ions and Cholesterols, *Chem-Bio Informatics Journal*, 4, 15-26 (2004)

(3) Mori, K., Hata, M., Neya S., Hoshino, T.: Common Semiopen Conformations of Mg^{2+}-free Ras, Rho, Rab, Arf, and Ran Proteins Combined with GDP and Their Similarity with GEF-bound Forms, *Journal of American Chemical Society*, 127, 15127-15137 (2005)

本学位論文の審査は千葉大学大学院薬学研究院で指名された下記の審査委員により行われた。

主査	千葉大学教授（薬学研究院）薬学博士	戸井田　敏彦
副査	千葉大学教授（薬学研究院）薬学博士	小林　弘
副査	千葉大学教授（薬学研究院）薬学博士	堀江　利治